THE ASTROPHYSICAL JOURNAL, 979:35 (27pp), 2025 January 20 https://doi.org/10.3847/1538-4357/ad7e2b

PHAST. The Panchromatic Hubble Andromeda Southern Treasury. I. Ultraviolet and Optical Photometry of over 90 Million Stars in M31

Zhuo Chen[1], Benjamin Williams[1], Dustin Lang[2], Andrew Dolphin[3,4], Meredith Durbin[1,5], Julianne J. Dalcanton[1,6], Adam Smercina[1,7,21], Léo Girardi[8], Claire E. Murray[7,9], Eric F. Bell[10], Martha L. Boyer[7], Richard D'Souza[11], Karoline Gilbert[7,9], Karl Gordon[7], Puragra Guhathakurta[12], Francois Hammer[13], L. Clifton Johnson[14], Tod R. Lauer[15], Margaret Lazzarini[16], Jeremiah W. Murphy[17], Ekta Patel[18,21], Amanda Quirk[19], Mariangelly Díaz Rodríguez[17], Julia Christine Roman-Duval[7], Robyn E. Sanderson[20], Anil Seth[18], Tobin M. Wainer[1], and Daniel R. Weisz[5]

[1] Department of Astronomy, Box 351580, University of Washington, Seattle, WA 98195, USA; zczhuo@uw.edu
[2] McWilliams Center for Cosmology, Department of Physics, Carnegie Mellon University, 5000 Forbes Ave., Pittsburgh, PA, USA
[3] Raytheon, Tucson, AZ 85756, USA
[4] Steward Observatory, University of Arizona, Tucson, AZ 85726, USA
[5] Department of Astronomy, University of California Berkeley, Berkeley, CA 94720, USA
[6] Center for Computational Astrophysics, Flatiron Institute, 162 Fifth Ave., New York, NY 10010, USA
[7] Space Telescope Science Institute, 3700 San Martin Dr., Baltimore, MD 21218, USA
[8] Osservatorio Astronomico di Padova—INAF, Vicolo dell'Osservatorio 5, I-35122 Padova, Italy
[9] The William H. Miller III Department of Physics & Astronomy, Bloomberg Center for Physics and Astronomy, Johns Hopkins University, 3400 N. Charles St., Baltimore, MD 21218, USA
[10] Department of Astronomy, University of Michigan, 1085 S. University Ave., Ann Arbor, MI 48109-1107, USA
[11] Vatican Observatory, Specola Vaticana V-00120, Vatican City State
[12] Department of Astronomy and Astrophysics, University of California Santa Cruz, University of California Observatories, 1156 High St., Santa Cruz, CA 95064, USA
[13] GEPI, Observatoire de Paris, Paris Sciences et Lettres, CNRS, Place Jules Janssen, F-92195 Meudon, France
[14] Center for Interdisciplinary Exploration and Research in Astrophysics (CIERA) and Department of Physics and Astronomy, Northwestern University, 1800 Sherman Ave., Evanston, IL 60201, USA
[15] NOAO, 950 North Cherry Ave., Tucson, AZ 85721, USA
[16] Department of Physics and Astronomy, California State University, Los Angeles, CA 90032, USA
[17] Department of Physics, Florida State University, 77 Chieftan Wy., Tallahassee, FL 32306, USA
[18] Department of Physics and Astronomy, University of Utah, 115 South 1400 East, Salt Lake City, UT 84112, USA
[19] Department of Astronomy, Columbia University, 538 West 120th St., New York, NY 10027, USA
[20] Department of Physics & Astronomy, University of Pennsylvania, Philadelphia, PA 19104, USA

Received 2024 June 7; revised 2024 July 11; accepted 2024 July 16; published 2025 January 16

Abstract

The Panchromatic Hubble Andromeda Southern Treasury (PHAST) is a large 195-orbit Hubble Space Telescope program imaging ~0.45 deg^2 of the southern half of M31's star-forming disk at optical and near-ultraviolet (NUV) wavelengths. The PHAST survey area extends the northern coverage of the Panchromatic Hubble Andromeda Treasury (PHAT) down to the southern half of M31, covering out to a radius of ~13 kpc along the southern major axis and in total ~two-thirds of M31's star-forming disk. This new legacy imaging yields stellar photometry of over 90 million resolved stars using the Advanced Camera for Surveys in the optical (F475W and F814W), and the Wide Field Camera 3 (WFC3) in the NUV (F275W and F336W). The photometry is derived using all overlapping exposures across all bands, and achieves a 50% completeness-limited depth of F475W ~ 27.7 in the lowest surface density regions of the outer disk and F475W ~ 26.0 in the most crowded, high surface brightness regions near M31's bulge. We provide extensive analysis of the data quality, including artificial star tests to quantify completeness, photometric uncertainties, and flux biases, all of which vary due to the background source density and the number of overlapping exposures. We also present seamless population maps of the entire M31 disk, which show relatively well-mixed distributions for stellar populations older than 1–2 Gyr, and highly structured distributions for younger populations. The combined PHAST + PHAT photometry catalog of ~0.2 billion stars is the largest ever produced for equidistant sources and is available for public download by the community.

Unified Astronomy Thesaurus concepts: Galaxies (573); Andromeda Galaxy (39); Stellar populations (1622); Local Group (929); HST photometry (756)

Materials only available in the online version of record: machine-readable tables

1. Introduction

The Local Group serves as a nearby laboratory for studying the astrophysics that controls the formation and evolution of galaxies. The Hubble Space Telescope (HST) is capable of resolving hundreds of millions of stars within Local Group galaxies, with well-measured distances and well-characterized foreground extinction. Such large libraries of resolved stellar

---

[21] Hubble Fellow.

photometry provide some of the most detailed data available to constrain fundamental astrophysical quantities and processes including the initial mass function (IMF; e.g., N. Bastian et al. 2010; D. R. Weisz et al. 2015), star formation (e.g., J. Harris & D. Zaritsky 2004, 2009; E. Sabbi et al. 2007; M. Cignoni et al. 2010; D. R. Weisz et al. 2011), stellar evolution (e.g., C. Gallart et al. 2005; P. Rosenfield et al. 2014; M. L. Boyer et al. 2019), feedback into the interstellar medium (ISM; e.g., K. B. W. McQuinn et al. 2010; A. M. Stilp et al. 2013; J. Peltonen et al. 2023), chemical enrichment (e.g., E. Tolstoy et al. 2009), distance scale (e.g., M. K. Barker et al. 2004; A. W. McConnachie et al. 2005), dust production (e.g., R. Schneider et al. 2014; M. L. Boyer et al. 2017), and galaxy formation and evolution (e.g., E. D. Skillman et al. 2003; B. F. Williams et al. 2009a; M. R. L. Cioni et al. 2011; J. J. Dalcanton et al. 2012; Y. Choi et al. 2018)—all of which are required for interpreting observations across cosmic time.

As the nearest spiral galaxy to the Milky Way and the largest galaxy in the Local Group (e.g., A. W. McConnachie 2012), the Andromeda galaxy (M31) is the only large metal-rich spiral besides the Milky Way for which we can resolve stars in the disk fainter than the information-rich horizontal branch. Detailed population studies of M31 have similar scientific potential. M31 studies circumvent complications from line-of-sight reddening, uncertain distances, and background/foreground confusion. Furthermore, such studies can be put into the context of the surrounding local environment, such as the ISM structure, the star formation rate (SFR), and the metallicity of the stars and gas, and even larger environment as mapped by the Pan-Andromeda Archeological Survey (e.g., R. A. Ibata et al. 2014). Thus, M31 provides a unique and interesting comparison to the detailed information we have for our Milky Way.

While both the Milky Way and M31 are "green valley" galaxies, which may be in the process of quenching (S. J. Mutch et al. 2011), many other aspects of the galaxies differ significantly. For example, these two galaxies are remarkably different in their detailed disk and halo structure and kinematics, suggesting that they have followed significantly different evolutionary tracks. The M31 halo is aglow with streams (R. A. Ibata et al. 2014), while that of the Milky Way is comparatively smooth with relatively fainter streams (A. J. Deason et al. 2011). The stellar disk of M31 is surprisingly thick (e.g., M. L. M. Collins et al. 2011; C. E. Dorman et al. 2015; J. J. Dalcanton et al. 2023), in stark contrast to that of the Milky Way (e.g., J. Bovy et al. 2012). The structure of the M31 disk is more ring-like than spiral-like (K. D. Gordon et al. 2006; A. R. Lewis et al. 2015). The gas fraction in M31 is approximately half that of the Milky Way (H. Nakanishi & Y. Sofue 2003; E. Corbelli et al. 2010), and its SFR is also roughly half that of the Milky Way (B. F. Williams 2003; T. P. Robitaille & B. A. Whitney 2010; A. R. Lewis et al. 2015; B. F. Williams et al. 2017; D. Elia et al. 2022).

In the past decade, detailed stellar population analyses have converged on a potential cause for the vast majority of these differences—a major merger event that rocked M31 2–4 Gyr ago (M. L. M. Collins et al. 2011; B. F. Williams et al. 2014, 2017; E. J. Bernard et al. 2015; C. E. Dorman et al. 2015; R. D'Souza & E. F. Bell 2018; F. Hammer et al. 2018; I. Escala et al. 2020, 2021; M. Arnaboldi et al. 2022; J. J. Dalcanton et al. 2023). Thus, M31 may provide our best opportunity for detailed measurements, comparable in quality to simulations, of the effects of mergers on such massive disks, including the possible role of mergers in pushing disk galaxies off the star-forming sequence and into quiescence.

The northern half of M31's disk has been successfully mapped in the Panchromatic Hubble Andromeda Treasury (PHAT; J. J. Dalcanton et al. 2012; B. F. Williams et al. 2014). The PHAT program covered roughly one-third of the entire star-forming disk of M31 in six bands ranging from the near-ultraviolet (NUV) to the near-infrared (NIR). The resulting star catalogs have extensive legacy value with broad reach and have already demonstrated the scientific impact of these resolved stellar populations. Some examples include star clusters and their formation processes (L. C. Johnson et al. 2015, 2017), stellar halo structure (B. F. Williams et al. 2015), the longevity of star-forming regions and dissemination of young stars (A. R. Lewis et al. 2015), galactic disk formation and evolution (A. R. Lewis et al. 2015; B. F. Williams et al. 2017), the history of the Local Group (R. D'Souza & E. F. Bell 2018; F. Hammer et al. 2018), the IMF (D. R. Weisz et al. 2015), calibration of SFR indicators (A. R. Lewis et al. 2017), dynamical studies of M31's stellar disk with resolved spectroscopy (C. E. Dorman et al. 2013, 2015; A. Quirk et al. 2019; I. Escala et al. 2023), nova progenitors (M. Henze et al. 2018), metal retention (O. G. Telford et al. 2019), mass-to-light ratios (O. G. Telford et al. 2020), and dust mapping (J. J. Dalcanton et al. 2015, 2023).

While the northern disk survey has produced a wealth of information, the southern disk has had comparatively few detailed measurements. The southern disk appears fundamentally different from the region targeted by PHAT. Its features suggest the southern disk is more disturbed, and it has been more affected by M31's merger history (R. D'Souza & E. F. Bell 2018; F. Hammer et al. 2018). M32, a compact dwarf elliptical satellite, is projected just 5 kpc from the center of M31 against the southern disk. M32 has been proposed as the remnant of the progenitor which formed the giant southern stream (GSS; R. Ibata et al. 2001), a stream spanning ∼150 kpc extending outwards from the southern half of the disk (R. Ibata et al. 2007). Some scenarios suggest M32 is the core of the massive merged galaxy (e.g., K. Bekki et al. 2001; R. D'Souza & E. F. Bell 2018) that produced the stream, which would be consistent with the simultaneous burst of star formation seen in both M32 and M31 (A. Monachesi et al. 2011). However, other models suggest the stream's progenitor was completely disrupted (M. A. Fardal et al. 2006, 2007, 2013; F. Hammer et al. 2018). Consistent, uniform analyses of the stellar populations of M31, M32, and the GSS should be able to test for relative age differences and velocity signatures in their stellar populations, distinguishing among these models. A first step in such a process is the production of a deep resolved stellar photometry catalog.

Additional difference between M31's north and south is that the latter's star-forming regions have a more complex morphology, including key features of interest such as the largest star-forming region in M31 (NGC 206), and the most massive young cluster in M31 (e.g., S. Perina et al. 2009). These features further suggest that the southern half may have been more recently or more violently disturbed (K. D. Gordon et al. 2006).

Furthermore, a nonaxisymmetric velocity field in M31 between the northern and southern halves of the disk has been

Table 1
Sample Exposure Data for One Field

Target Name	R.A. (J2000)	Decl. (J2000)	Start Time	Exp. (s)	Inst.	Aperture	Filter	Orien.
M31-B24-F01-UVIS	$00^{h}43^{m}42^{s}.5$	$+41^{\circ}06'28''$	2023-01-01 07:16:21	178.0	WFC3	UVIS-CENTER	F336W	−67.1906
M31-B24-F01-UVIS	$00^{h}43^{m}42^{s}.5$	$+41^{\circ}06'28''$	2023-01-01 07:21:39	700.0	WFC3	UVIS-CENTER	F336W	−67.1893
M31-B24-F01-UVIS	$00^{h}43^{m}42^{s}.5$	$+41^{\circ}06'28''$	2023-01-01 07:36:00	720.0	WFC3	UVIS-CENTER	F275W	−67.1913
M31-B24-F01-UVIS	$00^{h}43^{m}42^{s}.5$	$+41^{\circ}06'28''$	2023-01-01 07:50:18	462.0	WFC3	UVIS-CENTER	F275W	−67.1955
M31-B24-F01-WFC	$00^{h}43^{m}06^{s}.7$	$+41^{\circ}09'19''$	2023-01-01 21:33:47	104.0	ACS	WFC	F814W	65.2573
M31-B24-F01-WFC	$00^{h}43^{m}06^{s}.7$	$+41^{\circ}09'19''$	2023-01-01 21:38:15	700.0	ACS	WFC	F814W	65.2587
M31-B24-F01-WFC	$00^{h}43^{m}06^{s}.7$	$+41^{\circ}09'19''$	2023-01-01 21:52:53	679.0	ACS	WFC	F475W	65.2574
M31-B24-F01-WFC	$00^{h}43^{m}06^{s}.7$	$+41^{\circ}09'19''$	2023-01-01 22:06:54	337.0	ACS	WFC	F475W	65.2543

(This table is available in its entirety in machine-readable form in the online article.)

reported, attributed to the presence of a bar (B. J. Gibson et al. 2023). The southern disk has a velocity that is more cleanly separated from the Milky Way than that of the northern disk. Because it is rotating toward us, the velocities of both stars and interstellar gas separate more easily from those of the Milky Way foreground (∼400–500 km^{-1}; E. Bajaja & W. W. Shane 1982). This separation simplifies any dynamical analyses compared to those of the northern disk covered by PHAT (e.g., C. E. Dorman et al. 2013; K. M. Howley et al. 2013; C. E. Dorman et al. 2015; A. Quirk et al. 2019).

To allow all of this potential science return, we have created a southern complement to the PHAT survey. The Panchromatic Hubble Andromeda Southern Treasury (PHAST) survey covers key diagnostic features sensitive to M31's complex merger history that were unconstrained by the northern disk observations alone. The PHAST survey is contiguous with PHAT, although it is designed to improve survey efficiency by dropping the infrared observations included in PHAT. This paper presents the PHAST survey's four-band resolved stellar photometry catalog. Section 2 describes the observing strategy and data reduction techniques. In Section 3, we present the resulting catalog of four-band panchromatic photometry of the resolved stars, along with investigations of the photometric quality via artificial star tests (ASTs). We present seamless stellar population maps of the entire M31 disk with the most distinct features in Section 4. Throughout the paper, we assume a distance to M31 of 785 kpc ($m-M=24.47$; A. W. McConnachie et al. 2005).

2. Observations and Data Analysis

The observations that comprise the PHAST survey were obtained over a long period of time and required extensive data acquisition and analysis, which we describe in the following subsections. We start with an overview of the survey and observing strategy. We then discuss our newly developed cosmic-ray (CR) rejection and astrometric alignment routine, followed by the details of our point-spread function (PSF) photometric measurement technique, and the ASTs for assessing photometric quality.

2.1. Survey Overview/observing Strategy

The observations for the PHAST program (GO-16778 and 16796–16801) were obtained from 2021 December 8 to 2024 January 13 using the Advanced Camera for Surveys (ACS) Wide Field Channel (WFC) and the Wide Field Camera 3 (WFC3) UVIS (ultraviolet) channel. All the HST data presented in this paper can be found in the Mikulski Archive for Space Telescopes (MAST) at the Space Telescope Science Institute at DOI:10.17909/6889-kg02. The observing strategy for the PHAST survey builds on the techniques developed by the PHAT survey (J. J. Dalcanton et al. 2012) of the northern half of M31 and the PHAT Triangulum Extended Region (PHATTER; B. F. Williams et al. 2021) survey of the inner disk of M33. PHAST utilizes a similar but more efficient tiling strategy at the cost of omitting the NIR filters that PHAT and PHATTER included. We reduce PHAT's two-orbit visits to a single orbit per pointing for PHAST. The observations use the larger UVIS footprint as the survey's fundamental coverage unit, rather than the smaller WFC3/IR footprint used in PHAT. The single-orbit visits are similar to the UVIS orbits of the PHAT program, but in PHAST, ACS takes both the F475W and F814W filters during that orbit. In total, 195 single-orbit visits observed in four filters. PHAST extends ∼13 kpc along the southern major axis of M31's disk, which does not reach as far as PHAT's radial coverage out to ∼17.5 kpc. Considering all these factors, the PHAST program required less than a quarter of the PHAT observing time. This observing strategy does sacrifice NIR photometry, which is useful for dust mapping (J. J. Dalcanton et al. 2015, 2023) and cool star observations (M. L. Boyer et al. 2017, 2019), and involves less repeat optical photometry and single exposure covering the ACS chip gap. However, NIR capability can potentially be added later with a small amount of Roman Space Telescope (R. Akeson et al. 2019) or Euclid (L. Amendola et al. 2018) time. The PHAT and PHAST surveys together cover ∼two-thirds of M31's star-forming disk. This estimation is based on the fraction of far-ultraviolet (FUV) flux from the Galaxy Evolution Explorer (GALEX; D. A. Thilker et al. 2005) enclosed within the entire survey footprint compared to the total flux from the whole disk.

At each pointing in the survey, WFC3/UVIS observations in the F275W (covering 250–300 nm) and F336W (covering 310–360 nm) filters and ACS/WFC observations in F475W (covering 400–550 nm) and F814W (covering 700–950 nm) were taken in parallel in one orbit. All observations were taken at two orientations, separated by 180°, in order to maximize the survey coverage for all cameras and optimize the use of parallel exposures. A list of the target names, observing dates, coordinates, orientations, instruments, exposure times, and filters is given in Table 1. In total, the PHAST survey covers a contiguous area of ∼1640 arcmin^2 in all four filters, including ∼13 kpc along the southern major axis of M31, as shown in Figure 1.

Each survey pointing is described by two identifiers, a brick number and a "field" number, following the naming convention

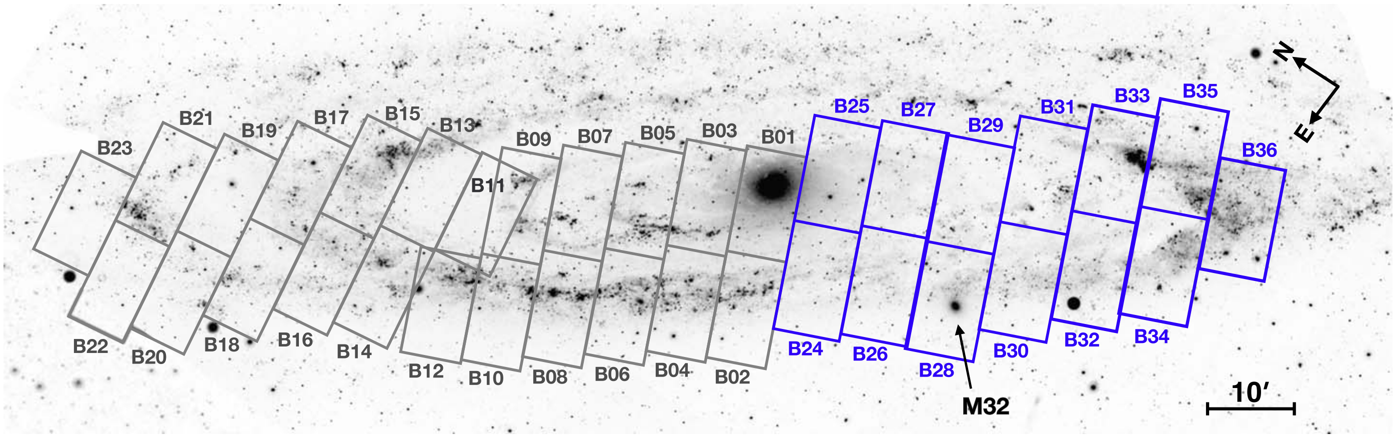

Figure 1. Locations of the 13 "bricks" of this new PHAST survey (blue outlines) and the 23 bricks of the PHAT survey (gray outlines), superimposed on a GALEX FUV image (D. A. Thilker et al. 2005). Each of the new PHAST bricks consists of 15 HST pointings (see Figure 2), each of which includes observations in two HST cameras. M32 is marked with an arrow in Brick 28.

used in PHAT (see more details in J. J. Dalcanton et al. 2012; B. F. Williams et al. 2014). The rectangular bricks are areas of ∼12.′5 × 7.′5 that correspond to a 5 × 3 array of WFC3/UVIS footprints (see Figure 1). This coverage of 15 pointings in one PHAST brick is larger than the PHAT survey brick of ∼12′ × 6′, which is covered in a 6 × 3 array of 18 pointings. This is because each PHAST pointing covers one UVIS footprint instead of one smaller IR footprint. Furthermore, as each pointing requires only one orbit of observations, the PHAST brick requires only 15 orbits instead of the 36 required per brick by the two-orbit observations of PHAT.

In total, the 13 PHAST bricks are numbered, 24–36, following the naming convention used in PHAT, which covered the first 1–23 bricks, with odd numbers for bricks along the major axis and larger increasing numbers with increasing distance from the center (see Figure 1). Within each of the 13 bricks in PHAST, each WFC3/UVIS pointing area is given a field number, 1–15, from the northeast corner, counting east to west, north to south, as shown in Figure 2. Thus, each WFC3/UVIS pointing has its own unique brick and field number. Parallel images in the ACS/WFC camera are labeled by the brick and field of the primary observations of UVIS footprint. The list of target names in Table 1 present the brick and field numbers of each pointing from each camera.

The overall survey footprints and tiling strategy are shown in the exposure maps in Figure 3. This tiling was designed to maximize the contiguous WFC3/UVIS coverage and make the most efficient use of the ACS/WFC parallels. The orientation of two pointings in Brick 31 and one pointing in Brick 35 were shifted due to a lack of available guide stars in the standard orientation. We adopted a similar exposure sequence (see Table 1) and dithering strategy to those in PHAT, and obtained two exposures in each filter. The adopted dithers are designed to improve the pixel sampling in F475W and F814W, but do not fill in the ACS chip gap. Instead, the ACS chip gaps are only filled by overlapping exposures from observations in adjacent fields. The two WFC3/UVIS exposures for each filter are dithered to fill the chip gap. Our dithering included a half pixel along the diagonal in order to recover as much spatial resolution possible. Note that the majority of the chip gap is only imaged in one exposure per filter, making CR rejection more challenging in this region. We helped to develop a CR masking routine to mitigate this consequence of our observing strategy, see Section 2.2 and Z. Chen et al. (2024).

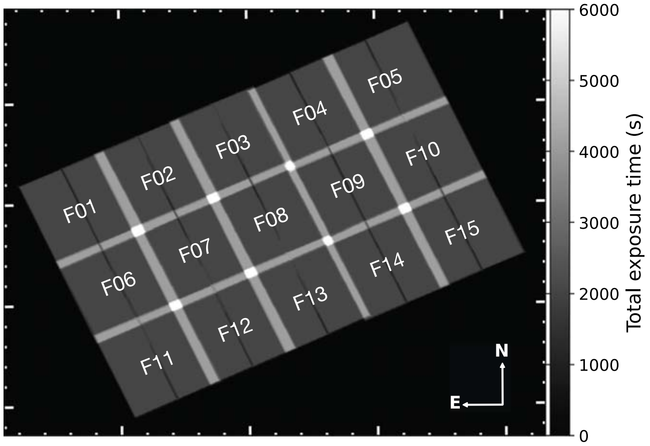

Figure 2. WFC3/UVIS exposure map with labeled field numbers for 15 pointings across a generic PHAST brick. The gray scale indicates the amount of total exposure at each location in seconds. The WFC3/UVIS exposures are dithered to cover the chip gap.

The resulting map of exposure times in each camera is shown in Figure 3. Because the majority of the observations in the optical are crowding limited, rather than photon limited, the PHAST survey reaches a similar detection depth as PHAT in the crowded inner regions near the bulge. Outside of this, where the observations were no longer crowding limited, our photometry is not as deep as PHAT, but still reaches below the information-rich red-clump (RC) feature critical for finding differences between old populations. The varying exposure times due to the overlapping pointings tend to affect the photometry in less obvious ways that are often only noticeable at faint magnitudes.

To optimize our photometric depth throughout the survey, we included all overlapping exposures when measuring photometry. The large amount of overlap between neighboring ACS fields effectively collects two orbits of observations in most areas covered by ACS, which allows for a final optical mosaic comparable in quality to the current PHAT mosaic. See Section 2.2.2 for more details. The full resolution combined images are also available at MAST as part of a High Level Science Product (HLSP) via DOI:10.17909/aa43-mt38.

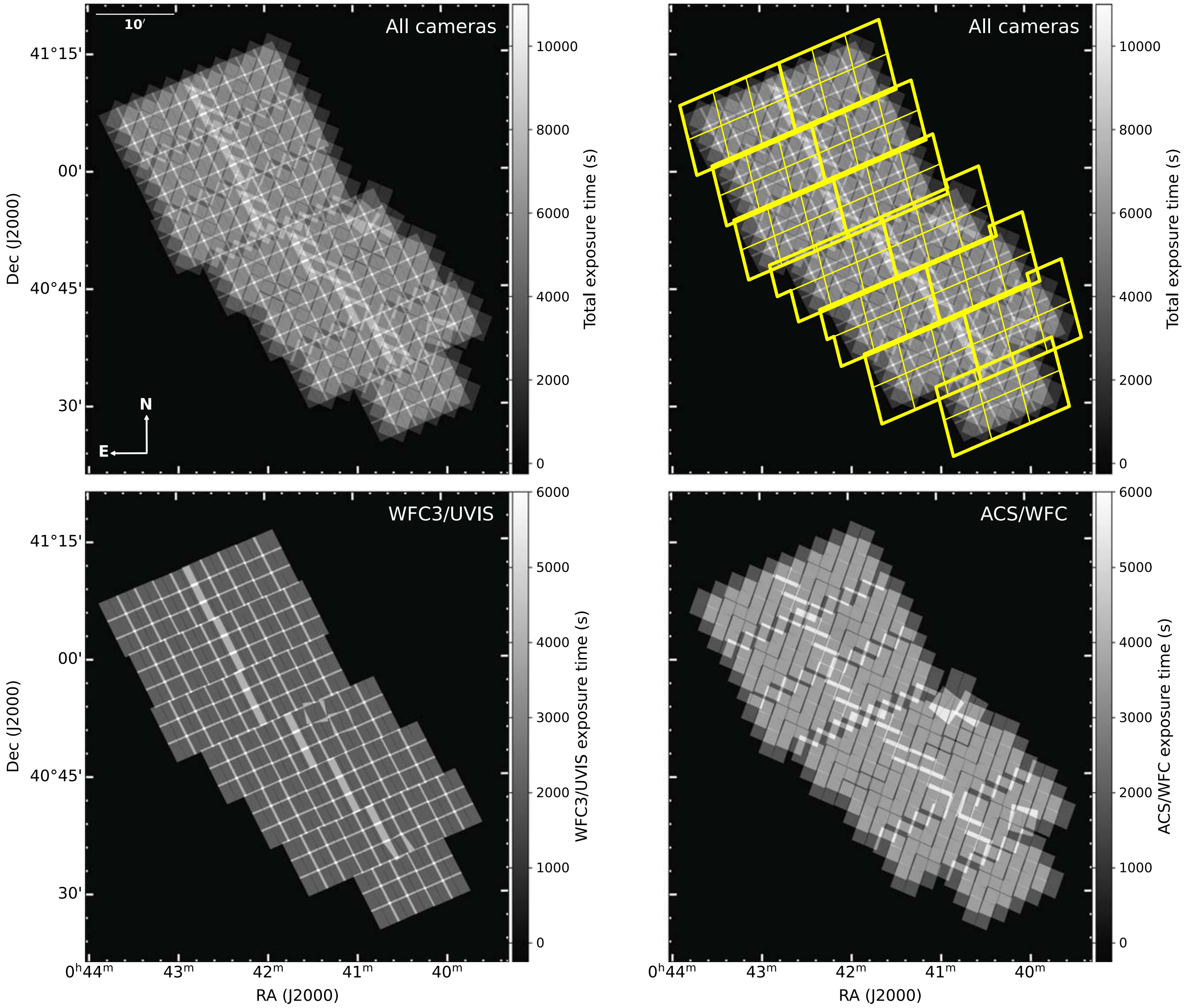

Figure 3. Top left: exposure map of the entire survey for two cameras (WFC3/UVIS and ACS/WFC). The gray scale indicates the amount of total exposure at each location in seconds. The orientation of three pointings were shifted due to a lack of available guide stars in the standard orientation. Top right: the yellow outlines display how the observations were divided for processing. Each brick (thicker line) was divided into six subregions, totaling 78 analysis regions for the entire survey. Bottom left: exposure map for WFC3/UVIS only. Bottom right: exposure map for ACS/WFC only.

2.2. Cosmic-Ray Rejection and Astrometric Alignment

The downloaded calibrated images used for all of our analysis were processed under OPUS versions 2016_2-2017_3b. For all of our analysis, we start with the charge transfer efficiency (CTE)-corrected (J. Anderson & L. R. Bedin 2010; J. Anderson & J. E. Ryon 2018) `*flc.fits` image files.

We aligned all of the 780 ACS/WFC and 780 WFC3/UVIS `*flc.fits` individual exposures to the Gaia Data Release 2 (DR2) astrometric solution. These two cameras, ACS and WFC3, have different challenges when aligning images with astrometric corrections. Most of the original ACS `*flc.fits` single-exposure images in the optical, directly downloaded from the MAST, already have well-corrected astrometry aligned to Gaia via the MAST data reduction pipeline. The high density of sources in our ACS optical images facilitates astrometric correction, with sufficient stars serving as reference sources for alignment between our images and the Gaia catalog. Thus, the high-density optical images also have a better cross correlation between the source positions in overlapping frames, making it easier to determine precise relative alignment shifts. The abundance of reference sources in our ACS images also makes them less susceptible to CR artifacts, which require more careful removal in UV images, where they often outnumber the stars. Out of a total of 780 ACS single-exposure frames, only eight frames required additional astrometry correction beyond their default headers from MAST.

In contrast to the crowded optical images, the sparse UV images often suffered from a relatively low number of real source detections (B. F. Williams et al. 2021), which could easily be outnumbered by the large number of CRs. The misidentification of CR artifacts as real sources led to difficulties in aligning objects across images, and this misalignment caused real sources to be mislabeled as CRs due to their inconsistent locations between pointings. Our astrometry correction routine builds on the workflow initially presented by V. Bajaj (2017) and applied in the PHATTER survey (B. F. Williams et al. 2021). This routine was designed to align stellar sources extracted from HST images to reference catalogs queried from Gaia. This workflow is especially helpful for cases where data have been taken at many pointings, but it can fail if there is a large fraction of artifacts in the raw images. Moreover, achieving good alignments still requires effective source detection in the input images, and this workflow specifically demands custom parameter selection depending on the quality of the input data, which was particularly challenging for our UV images. In this work, we have further improved the astrometric solution by performing CR masking and flagging bad pixels to clean all of the raw UV images (and a few ACS images) before astrometric alignment. We summarize the new workflow below.

2.2.1. Cosmic-Ray Masking

The original single-exposure UV images, as initially downloaded from the MAST, did not have well-determined CRs via the standard reduction and calibration, partially due to our observing strategy, which had only two exposures per band in UVIS. Previously, the PHAT and PHATTER surveys carried out the legacy method for CR flagging using the `AstroDrizzle` function from the `Drizzlepac` package (STSCI Development Team 2012; W. J. Hack et al. 2013; R. J. Avila et al. 2015). `AstroDrizzle` detects CRs by identifying pixels that exhibit brightness in one exposure but not in the other exposures in the same band. However, despite undergoing CR flagging via `AstroDrizzle`, the resultant images still retain a notable amount of CR contamination especially in UV images, and particularly in regions of reduced exposure coverage in a given dither pattern, such as the chip gap.

Instead, we introduced a novel approach for CR labeling and rejection through retraining the deep-learning-based CR masking routine `deepCR` (K. Zhang & J. S. Bloom 2020) to be optimal for UVIS, which is described in detail in Z. Chen et al. (2024). In brief, `deepCR` was applied to a given input `*flc.fits` image from WFC3/UVIS, generating a probability map of CRs. This probability map was then converted into a binary CR mask using a user-defined cutting threshold, with one representing CRs and zero representing nonartifacts. Through comprehensive performance assessments, a `deepCR` masking threshold of 0.1 was determined to be optimal for our survey observations, as it reliably identified CRs while minimizing the chance of incorrectly eliminating real objects. The potential contamination of flagged CR pixels by real stars is below 1% (see Figure 3 in Z. Chen et al. 2024), serving as an upper limit on the false positive rate of this method. This false flagging rate will be further reduced with the use of more exposures across additional filters, aiding in better identification of real stars in the images. For further information, see Z. Chen et al. (2024) for a detailed comparison of `deepCR` CR labeling and rejection examples on our PHAST UVIS images.

2.2.2. Astrometric Alignment and Mosaic Production

The binary CR mask was then applied to replace the flagging in the data quality (DQ) extension of the input image. We performed the PSF fitting photometry using the DOLPHOT software package (A. E. Dolphin 2000; A. Dolphin 2016) in single mode on the `deepCR` CR-flagged image to measure the positions of stars on each CCD of each exposure of the survey, during which the DQ flags were applied to the science (.SCI) extensions to mask out bad pixels and CRs. See more details of the photometry in Section 2.3. For each image, the resulting stellar catalog was then aligned to a reference astrometric catalog retrieved from the Gaia archive with `astroquery` (A. Ginsburg et al. 2017, 2019). These alignment was performed with the `TweakReg` function in the `Drizzlepac` package (STSCI Development Team 2012; W. J. Hack et al. 2013; R. J. Avila et al. 2015). The image header was updated with the resulting aligned astrometric solution, which was typically derived from several hundred stars per pointing.

Compared to the original workflow, our updated routine reliably aligns single exposures if needed and does not require large mosaics or data sets with multiple pointings to remove artifacts. Additionally, we found that this new routine eliminates the need for dedicated testing to determine the optimal set of parameters used for the `TweakReg` function for each exposure, including thresholds for source detection and error budgets for Gaia sources. For our entire survey, we were able to apply a uniform, optimal set of parameters. We used this updated routine to correct all of our UVIS images and a few ACS exposure that required additional astrometric correction.

We then used the `AstroDrizzle` function of the `Drizzlepac` package to combine our CR-masked, astrometrically aligned individual images within each band into a distortion-corrected, high-resolution pixel array ($0\farcs035$ pixel^{-1} in both bands, combined with a `lanczos3` kernel). This higher-resolution array allows the full camera resolution to be recovered from dithered images, which were subpixel sampled in F475W, F814W, and F336W. Of particular note, the DQ extensions of the individual exposures would be further updated in this `AstroDrizzle` step when multiple pointings are available, flagging additional CRs and bad pixels which were not recognized in the single-exposure `deepCR` step. A `minmed` filter flagged statistical outlier pixels on the input exposures for all filters. These pixels were also masked when generating the combined image, as well as in all further analysis. The images were then combined with `astrodrizzle` to produce deep mosaics that take advantage of subpixel dithering to improve spatial resolution. See Section 2.3.5 for examples of deep mosaics at different stellar densities.

2.3. Photometry

PSF fitting at the location of each source detected in our survey footprint was used to derive photometric measurements. Apart from the CR rejection and astrometric improvements we have made in aligning the images (Section 2.2), we closely followed the photometry process applied to the PHAT legacy photometry (B. F. Williams et al. 2023) and the PHATTER survey (B. F. Williams et al. 2021) to simplify comparisons. A high-level overview of the process of measuring the stellar photometry is provided as follows.

All 1560 individual exposures were aligned to the Gaia DR2 astrometric solutions and combined into mosaic images (see more details in Section 2.2). The flagged bad pixels and pixels affected by CRs were masked out during the photometry. The aligned individual images were processed with the DOLPHOT software package (A. E. Dolphin 2000; A. Dolphin 2016) to measure PSF corrections and aperture corrections, which largely correct for variations in telescope focus. All overlapping individual exposures within each subregion were stacked in memory, to search for all statistically significant detections using the full survey depth. At each detected centroid, the appropriate PSF was fit to the detection's locations in each of the overlapping exposures, for all filters simultaneously. DOLPHOT then reported the measured fluxes and corresponding magnitudes in each image, as well as the combined flux and magnitude in each observed band. Finally, the raw photometry output was processed to flag possible artifacts and generate summary catalogs containing a subset of the many thousands of columns required to describe the complete measurement suite.

We describe each of these steps in detail below.

2.3.1. Dividing the Data for Each Photometry Run

One difference between the PHAST photometry and that of PHAT and PHATTER was how data was divided for processing. To improve the reduction efficiency, we divided the data into separate subregion stacks to measure the photometry across different fields of the survey in parallel. We used the DOLPHOT parameters that allow a user-defined region within which the photometry is performed including all overlapping individual images. For each brick, we divided the data into six subregions, totaling 78 analysis regions for the entire survey. See Figure 3 (upper right panel) for the detailed design of all subregions. These subregions were sufficiently small that DOLPHOT could complete the PSF fitting photometry in a reasonable amount of clock time, typically about 1 week. The regions were also sufficiently large to avoid repeating the photometry fitting on one image in too many substacks. The subregions within a brick were specifically designed to overlap by at least $2''$ on a side to avoid introducing edge effects. The overlaps between bricks in the northwest (vertical) direction were introduced by the observing strategies. In each of these 78 photometry runs, as was done for PHATTER and PHAT, we include all of the exposures that overlapped at all with the subregion, even if they come from an adjacent brick. See Figure 4 for example of one subregion. Thus, neighboring subregion sets had many exposures in common, namely, all of the exposures that overlapped with the boundary, providing consistent photometry along all of the edges, as well as the deepest possible photometry inside of the subregion boundaries.

2.3.2. Preparing Individual Exposures

After updating the original `*flc.fits` images with new astrometry and DQ extensions, individual exposures were passed through our photometry pipeline, which requires several preprocessing preparation steps before running DOLPHOT for photometry. The preparation starts with running the task `acsmask` for ACS/WFC or task `wfc3mask` for WFC3/UVIS on each exposure. This task masks the flagged pixels in the DQ extensions of each CCD in each exposure, and multiplies the image by the appropriate pixel area map in order to take into account the distortion effects on the flux measured in each pixel. This step is also run on the full-depth F475W stacked image, which is the deepest band. DOLPHOT uses this stacked image as the astrometric reference frame, aligning all individual exposures to it in memory and reporting all final star positions based on this reference. As such, it is beneficial to use the deepest and highest spatial resolution image for this purpose.

We ran the task `splitgroups` to separate files for each CCD of each exposure, and then we ran the task `calcsky` on each of these individual frames and generate maps of the sky level in each exposure by simply smoothing the original images. These sky maps are used by DOLPHOT to generate an initial list of statistically significant centroids in order to align each individual frame to the astrometric reference image. These sky files are not actually used for measuring the true sky level in the photometry fitting, which instead will be measured in a much more sophisticated way described in Section 2.3.3. DOLPHOT was first run on each individual exposure to measure the central PSF and aperture corrections of each CCD read. Then we ran DOLPHOT's alignment on the full stack of CCD reads in order to determine and record the parameters that align each individual frame to the astrometric reference image. These alignment parameters will then be used to run final full-stack photometry for the entire survey, which will be described below in Section 2.3.3.

2.3.3. Running DOLPHOT on a Full Image Stack

The astrometry-corrected images, alignment parameters, PSF corrections, and aperture corrections for each individual exposure, as obtained from the previous steps, are used to run full-stack photometry for the entire survey. The photometry was run in each subregion (Section 2.3.1) across different fields of the survey in parallel to improve the reduction efficiency. We followed the same DOLPHOT parameters as those used in the PHAT legacy (B. F. Williams et al. 2023) and PHATTER (B. F. Williams et al. 2021) surveys to optimize the resulting catalogs for stellar populations science and simplify comparisons. The main improvements compared to the initial PHAT (B. F. Williams et al. 2014) are the removal of catalog-level CTE corrections, and the implementation of spatially varying TinyTim PSFs (J. E. Krist et al. 2011) for all cameras. We present all DOLPHOT parameters adopted for our PHAST survey reductions in Table 2. Figure 5 shows the resulting alignment scatter with respect to the reference image in milliarcseconds from each CCD read for both detectors, calculated by DOLPHOT, after our newly developed astrometry correction routine. The alignment scatter values peak at ~10 mas for ACS/WFC and ~15 mas for WFC3/UVIS.

2.3.4. Flagging and Processing Photometry Output

DOLPHOT returns a comprehensive table for all of the measurements made on every PSF fit to every image, as well as the combined measurement of every source in every filter. The final measurements include the count rate, count-based uncertainty, flux, Vega system magnitude and error, background, and signal-to-noise ratio (S/N). The outputs also report several measurements of how well the source was fitted by the PSF, including the quality metrics `sharpness`, `roundness`, χ, and `crowding`. Full descriptions of these are presented in the DOLPHOT documentation.[22] Briefly, Vega magnitudes apply the encircled energy corrections and zero-points from R. C. Bohlin (2016) for the ACS/WFC, and from S. E. Deustua et al. (2017) for the WFC3/UVIS. Measurements of count rate and rate error are especially valuable for stars undetected in one or more bands, leading to negative or zero rates and, consequently, an undefined magnitude. These measurements offer upper limits in such bands, which can be used as constraints when modeling spectral energy distributions (SEDs). The `sharpness` parameter quantifies the central

---

[22] http://americano.dolphinsim.com/dolphot/

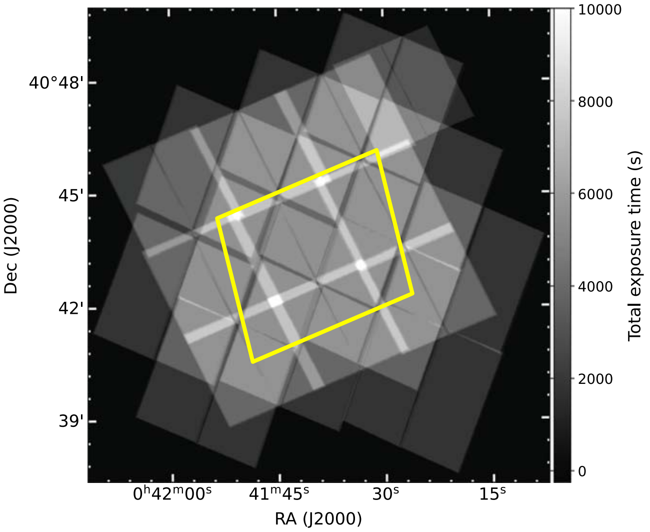

Figure 4. Map of all exposures included in a typical subregion run. The yellow box represents one of the 78 subregions shown in Figure 3. Photometry was performed only on the area indicated within the yellow box, but all exposures with pixels overlapping in these areas were included in the photometry run, resulting in our seamless final catalog.

concentration of a source relative to the PSF, or the degree to which its flux is focused in the central pixels as opposed to the outer ones. High values (positive) indicate a source with a significant central concentration, characteristic of hot pixels or CRs. Conversely, low values (negative) suggest a source with insufficient peaking, typical of blended stars or background galaxies. A `sharpness` value of zero denotes a perfect match with a star. The `crowding` parameter, expressed in magnitudes, indicates how much a star's photometry is affected by nearby stars during the measurement. A value of zero corresponds to an isolated star, unaffected by neighboring sources. A higher `crowding` value signifies a more densely populated area within the PSF radius with other sources, increasing the likelihood of systematic uncertainties in the reported magnitude due to the subtraction of neighboring stars. The `roundness` parameter quantifies the circularity of the source, where a value of zero indicates perfect roundness. χ provides an estimate of the overall goodness of fit to the PSF. Additionally, these measurements are also provided for each individual exposure as well, enabling studies on variability or investigations into artifacts that were not removed during our preprocessing steps. All measurements are recorded in an ASCII file with the extension *`.phot`.

For this PHAST catalog, we have adopted the same criteria of the DOLPHOT parameters as the originally established ones for the PHAT and PHATTER surveys (B. F. Williams et al. 2014, 2021), which were designed to identify good measurements of real stars. For a comprehensive explanation of how these criteria were determined, please refer to B. F. Williams et al. (2014). A summary of these criteria is provided here for convenience. The "ST" ("star") catalogs were constructed exclusively for sources with $S/N \geqslant 4$ and reasonable sharpness (see below) in at least one filter. The ST criteria aim to reduce the presence of noise spikes, CRs, and artifacts associated with saturated stars in our catalogs. This preliminary filter eliminated up to 20% of the objects from the initial DOLPHOT output. Measurements not featured in the ST files should be approached with extreme caution by users. The "GST" ("good star") catalogs were further created by applying specific culling parameters for each camera due to differences in pixel scale and PSF sampling. For the ACS, the criteria were `sharpness`$^2 < 0.2$ and `crowding`< 2.25; for the UVIS, the criteria were `sharpness`$^2 < 0.15$ and `crowding`< 1.3. These culling parameters were optimized and chosen as they offer a balance between eliminating a significant number of sources not associated with features in the color–magnitude diagram (CMD) and retaining a very high fraction of total measurements. This approach prevents excessive data culling while accepting a higher proportion of uncertain measurements and potential contaminants. See Section 3.2 for further results of the culling process.

Table 2
DOLPHOT Parameters Used for All Photometry

Detector	Parameter	Value
UVIS	raper	3
UVIS	rchi	2.0
UVIS	rsky0	15
UVIS	rsky1	35
UVIS	rpsf	10
WFC	raper	3
WFC	rchi	2.0
WFC	rsky0	15
WFC	rsky1	35
WFC	rpsf	10
ALL	apsky	15 25
ALL	UseWCS	2
ALL	PSFPhot	1
ALL	PSFPhotIt	2
ALL	FitSky	2
ALL	SkipSky	2
ALL	SkySig	2.25
ALL	SecondPass	5
ALL	SearchMode	1
ALL	SigFind	3.0
ALL	SigFindMult	0.85
ALL	SigFinal	3.5
ALL	MaxIT	25
ALL	NoiseMult	0.10
ALL	FSat	0.999
ALL	FlagMask	4
ALL	ApCor	1
ALL	Force1	1
ALL	Align	2
ALL	aligntol	4
ALL	alignstep	2
WFC	ACSuseCTE	0
UVIS	WFC3useCTE	0
ALL	Rotate	1
ALL	RCentroid	1
ALL	PosStep	0.1
ALL	dPosMax	2.5
ALL	RCombine	1.415
ALL	SigPSF	3.0
ALL	PSFres	1
ALL	psfoff	0.0
ALL	DiagPlotType	PNG
ALL	CombineChi	1
WFC	ACSpsfType	0
UVIS	WFC3UVISpsfType	0

2.3.5. Survey Catalog

We merged the photometry catalogs from all subregions to create a final catalog for the survey as done for the

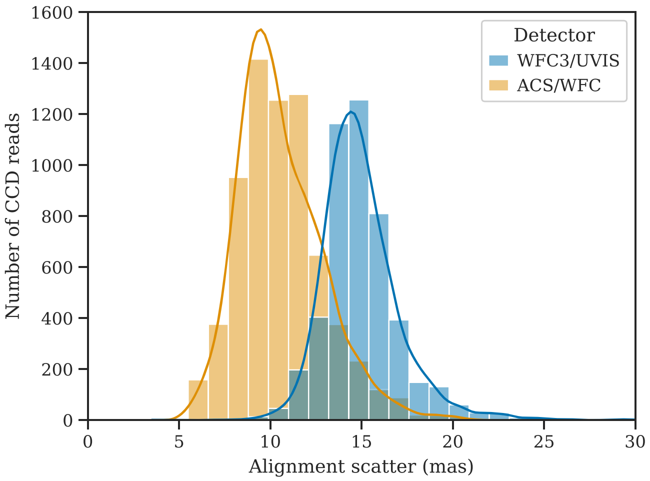

Figure 5. The resulting alignment scatter in units of mas from each CCD read for both detectors, calculated by DOLPHOT, after our newly developed astrometry correction routine. The alignment scatter values peak at ∼10 mas for ACS/WFC and ∼15 mas for WFC3/UVIS.

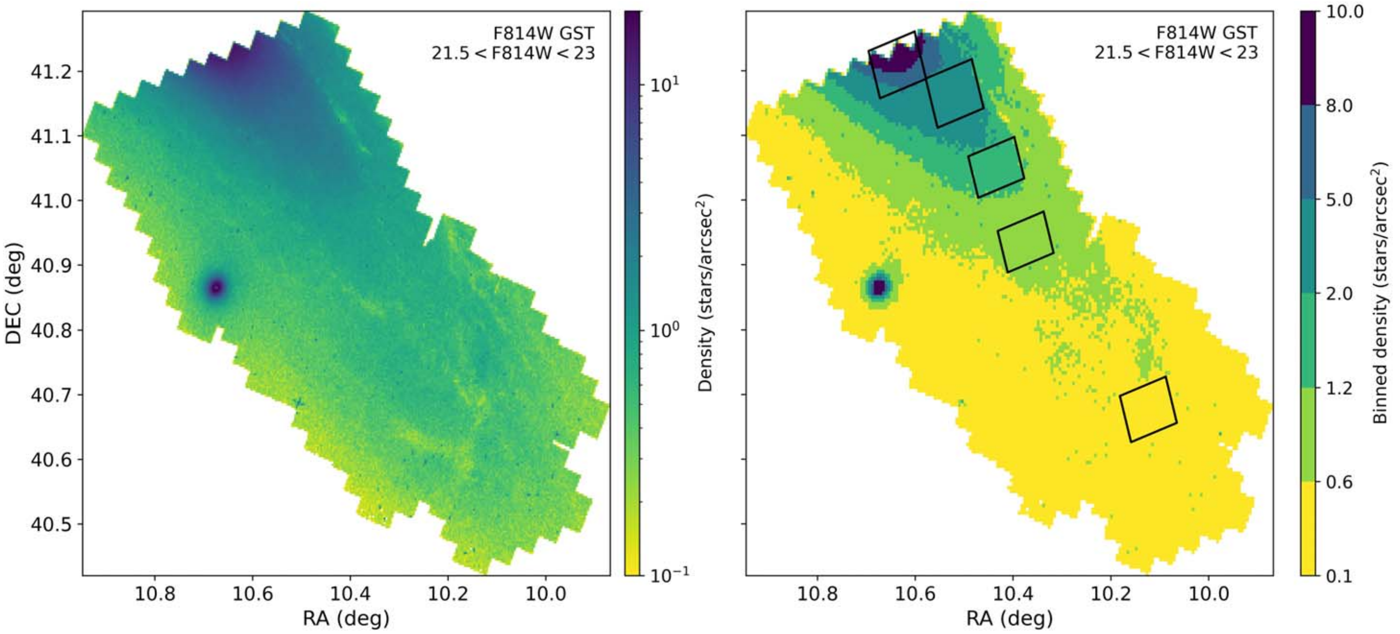

Figure 6. Left: map of the stellar density of the photometry catalog as determined by star counts per square arcsecond with $21.5 < \mathrm{F814W} < 23$, calculated in $10'' \times 10''$ pixels. Right: with the color map binned in six density bins. Black boxes mark the areas in which we have ASTs for determining the photometry quality (scatter, bias, and completeness) as a function of stellar density across the disk.

PHAT survey, keeping only one measurement for stars in the small overlaps between our defined regions (see more details in B. F. Williams et al. 2023). The source positions in the final PHAST catalog are precisely aligned with the Gaia DR2 astrometric solution. Using the stellar density distribution of the entire survey, we confirmed the absence of edge effects that could have been introduced by our processing divisions. Figure 6 illustrates the completeness-independent stellar density of the red giant branch (RGB), measured by counting the number of stars per square arcsecond with $21.5 < \mathrm{F814W} < 23$. While this is our adopted standard measure for stellar density, maps created without strict magnitude limits also showed no edge effects related to our processing divisions. The right panel of Figure 6 further displays the stellar density map binned into six density bins. Within these bins, the photometry quality (scatter, bias, and completeness) will be determined as a function of stellar density across the disk. Figure 7 bottom panels show the example color image mosaics for two regions in the disk with different stellar densities, utilizing the bands of F814W (red), F475W (green), and F336W (blue). The left region has a stellar density of ∼1.9 stars arcsec^{-2}, and the right region has a stellar density of ∼0.3 stars arcsec^{-2}.

We further integrated the catalogs from the overlapping regions between the PHAT and PHAST surveys to construct the complete photometry catalog for both surveys, collectively covering ∼0.91 deg^2 of the M31 disk. Of particular

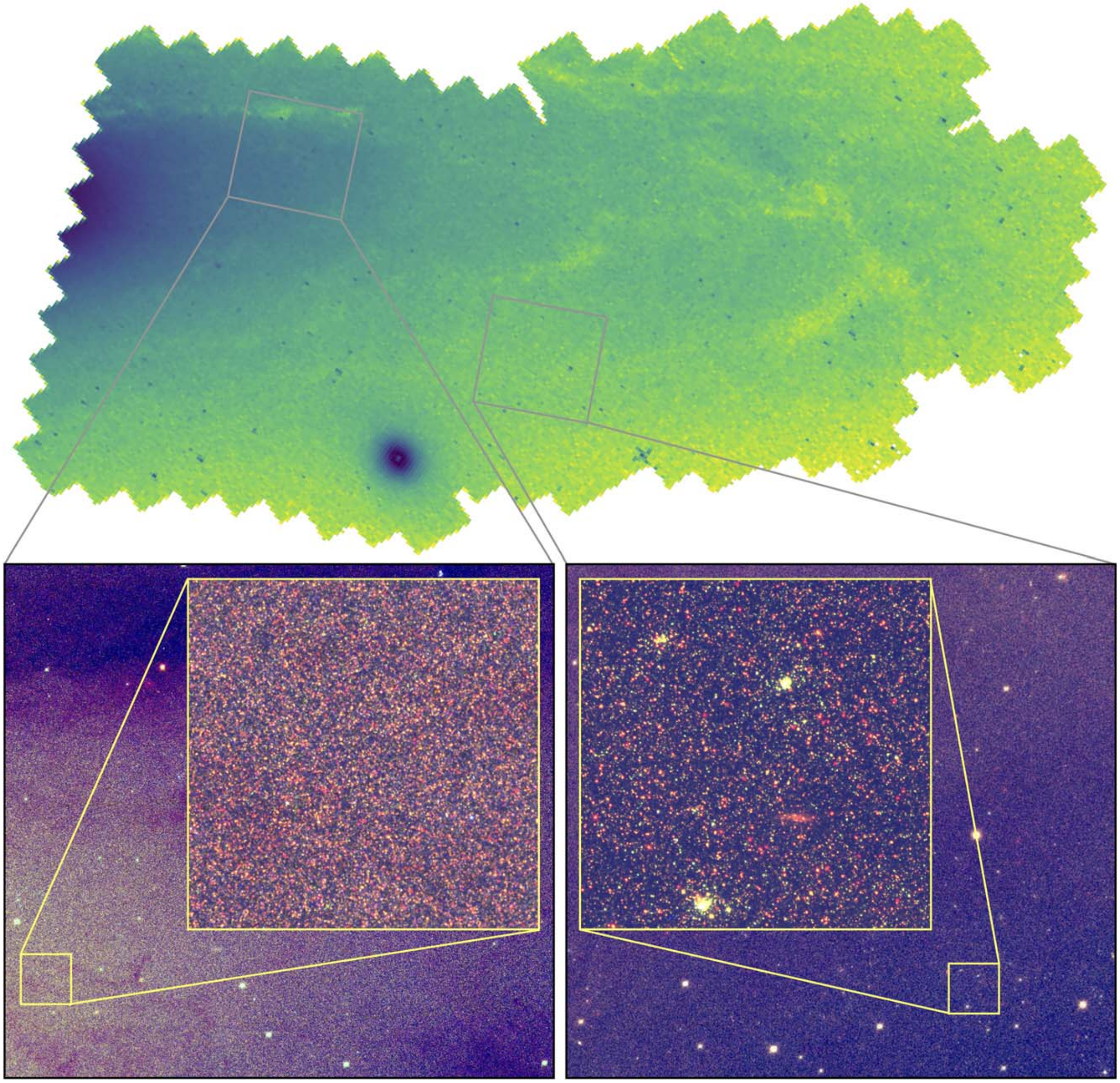

Figure 7. Top: stellar density map, identical to Figure 6 left panel. Bottom: three-color composite images for two regions in the disk with different stellar densities (left: ∼1.9 stars arcsec^{-2}; right: ∼0.3 stars arcsec^{-2}), utilizing the bands of F814W (red), F475W (green), and F336W (blue). The zoom-in panels highlight the rich detail available at full HST resolution. Each selection region is 5′.6 × 6′.0, and each inset zoom is 0′.55 × 0′.55.

note, the astrometric alignment in the PHAT survey was conducted before the release of the Gaia catalog (B. F. Williams et al. 2014). For optimal merging of the PHAT and PHAST catalogs, we recommend subtracting $2^\circ\!.21 \times 10^{-5}$ from the PHAT R.A. values and $1^\circ\!.67 \times 10^{-5}$ from the PHAT decl. values. Figure 8 displays the stellar density maps from both surveys. The left panel shows the density map of the optical GST stars brighter than F475W = 26, reaching roughly the completeness-limited depth for both surveys across the entire M31 disk, confirming no edge effects from different processing division designs. However, due to the observing strategy of the PHAST survey, the ACS chip gaps were only filled by overlapping exposures from observations from adjacent fields, leading to areas of reduced exposure in the chip gaps as shown in the stellar density maps at fainter magnitudes. The right panel of Figure 8 shows how exposure footprint features emerge at faint magnitudes, further highlighting the different tiling strategies of the two surveys. The one-orbit depth of our PHAST survey in the optical is slightly shallower in areas with fewer overlapping pointings than the two-orbit depth achieved by PHAT in the less crowded outer disk.

Our merging of the catalogs also allowed us to compare the PHAT and PHAST photometry directly. This consistency check of the photometry between the surveys shows excellent agreement (see Section 3.5).

In the final published high-level science products, we provide a catalog of the entire survey, as well as catalogs for each brick, with all of the measured DOLPHOT parameters for each detection.

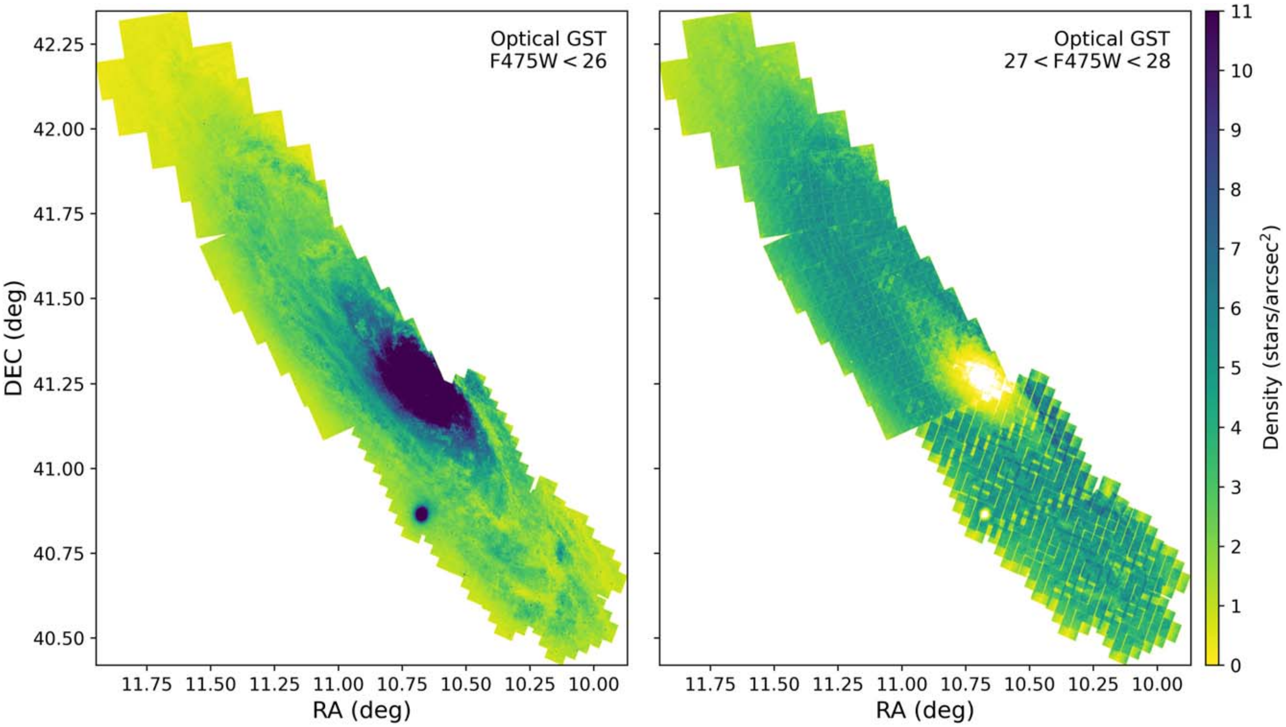

Figure 8. Stellar density maps of M31 from both PHAT and PHAST photometry catalogs. Left: optical GST stars with F475W < 26, which approximates the completeness-limited depth for both surveys across the entire M31 disk. Right: optical GST stars with 27 < F475W < 28. The varying exposure times due to the overlapping pointings have a more significant impact at fainter magnitudes. The exposure footprint features shown in the density map further reveal the different observing tiling strategies of the two surveys. The one-orbit depth of our PHAST survey in the optical is slightly shallower in areas with fewer overlapping pointings than the two-orbit depth achieved by PHAT in the less crowded outer disk.

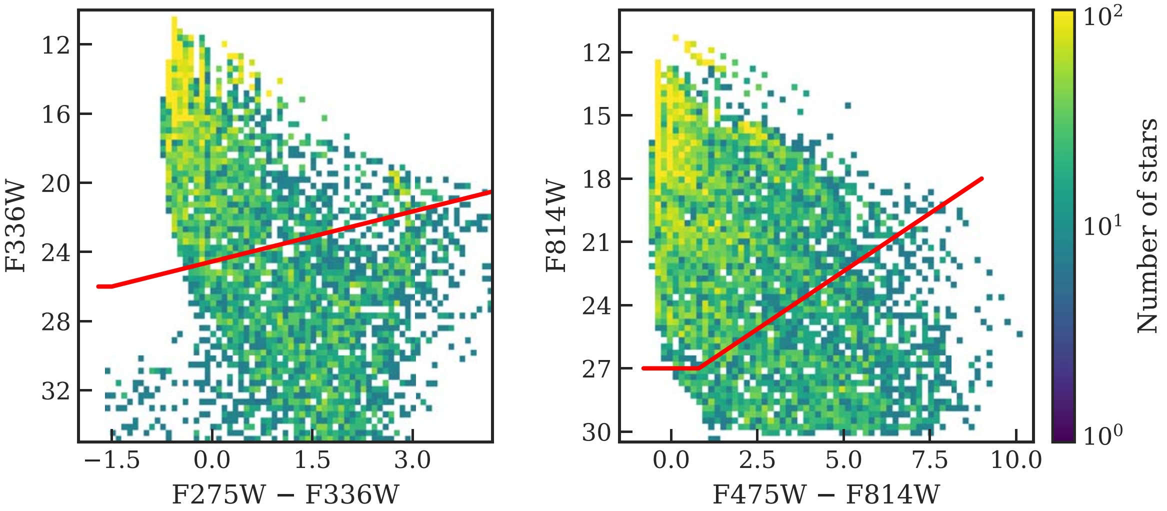

Figure 9. Input artificial star CMDs showing how the model SEDs cover the relevant color space. The color bar is in units of stars per CMD bin. Red lines mark the approximate depth of the observed photometry as seen from Figure 13.

2.4. Artificial Star Tests

We conducted a series of ASTs across various fields of this survey to quantify the precision, bias, and completeness of our photometry. Generally, these tests insert stars with realistic SEDs into fixed sky positions on each overlapping input image. These images are then processed through the same photometry routine as the original data to determine if the star is recovered and to compare the output photometry to the input. This procedure is carried out many thousands of times for a wide range of SEDs across various locations within the survey to evaluate the quality of our photometry catalogs as a function of color, magnitude and local stellar density.

We utilized the Bayesian Extinction and Stellar Tool (BEAST; K. D. Gordon et al. 2016) to generate SEDs across our four bands, creating a simulated artificial star photometry catalog. The SED models span a comprehensive grid of Padova/PARSEC models (P. Marigo et al. 2008; A. Bressan et al. 2012; P. Marigo et al. 2017), covering age ranges from 1 Myr to 13 Gyr and a metallicity range from $-2.1 < [\mathrm{Fe/H}] < -0.3$. These were combined with a Kroupa IMF (P. Kroupa 2001), random extinction levels ranging from $0 < A_V < 10$, and the distance to

Table 3
Sample Photometry Data[a]

R.A. (J2000)	Decl. (J2000)	F275W	S/N	GST	F336W	S/N	GST	F475W	S/N	GST	F814W	S/N	GST
10.917513	41.147666	99.999	0.0	F	99.999	0.0	F	99.999	0.0	F	16.689	259.3	T
10.922265	41.146577	99.999	0.0	F	99.999	0.0	F	18.697	276.8	T	17.562	314.0	T
10.934775	41.116702	17.951	63.4	T	16.550	134.0	T	99.999	0.0	F	99.999	0.0	F
10.932734	41.110273	18.448	49.3	T	17.585	18.5	T	99.999	0.0	F	16.482	383.4	T
10.914497	41.143193	99.999	0.0	F	99.999	0.0	F	18.475	506.9	T	18.251	163.3	T
10.882922	41.130832	99.999	0.0	F	99.999	0.0	F	18.941	384.0	T	17.561	362.6	T
10.892765	41.110199	19.856	48.8	T	18.417	104.2	T	18.232	471.1	T	17.076	418.9	T
10.924803	41.117321	22.367	18.6	T	19.084	80.1	T	99.999	0.0	F	99.999	0.0	F
10.920603	41.114629	20.800	18.9	T	19.014	60.3	T	18.491	327.3	T	17.188	413.6	T
10.886031	41.125301	25.429	2.7	F	21.339	27.0	T	18.937	561.6	T	99.999	0.0	F

Note.
[a] Vega magnitudes in all filters.
(This table is available in its entirety as part of a MAST HLSP via DOI:10.17909/aa43-mt38).

M31 (A. W. McConnachie et al. 2005). This approach ensures a broad color–magnitude space coverage, relevant to most of our photometry. The CMDs for the final AST inputs are displayed in Figure 9. To evaluate our photometric quality across each band, we included model stars extending at least 3 mag beyond the full magnitude range passing our quality cuts in each band. The scope of these AST inputs is sufficient for assessing completeness and precision based on magnitude for each observed band at a range of crowding levels.

We selected five subregions along the major axis that span the entire range of RGB stellar densities observed throughout the survey, as illustrated in Figure 6. For each designated region, we generated input lists of 50,000 artificial stars, each assigned random (X, Y) positions that follow the stellar density distribution of the original region. In total, we conducted 250,000 ASTs, covering 7% of the survey area. Each model SED of the input AST lists was applied with a photon noise simulation before being processed individually through our photometry routine as part of the ASTs, ensuring that the tests did not influence each other.

The output from DOLPHOT in AST mode provides the location and flux for each input star, alongside all other outputs reported for the unaltered data sets. The same quality metrics used to flag measurements in the star catalog were applied to the AST catalog to maintain consistency. An artificial star is deemed "recovered" in a specific band if its detected position is within two reference frame pixels ($0\farcs07$) of its input location, its magnitude is within 1 mag of the input value, and it meets the GST quality criteria for that band.

3. Results

3.1. Photometry Catalog

The full photometry catalog is available from the survey at MAST as part of a HLSP via DOI:10.17909/aa43-mt38. For examples, please refer to Table 3. This comprehensive photometry catalog provides the positions, Vega magnitudes, S/Ns, and DQ flags (uncertainty, χ, `sharpness`, `roundness`, `crowding`, error flag, etc.) for 90,885,399 stars. The source positions in the final PHAST catalog are precisely aligned with the Gaia DR2 astrometric solution, with a 2D scatter of the matching distance distribution that peaks at 4 mas. In cases where a star was not detected in a given band, the count rate and count rate error, which were derived from the sky background level, serve as constraints for a nondetection. Such nondetections are recorded in the magnitude column with a value of 99.999. This catalog presents all stars detected and measured by DOLPHOT, and for convenience, we have included a GST flag column for each band. This flag indicates stars with reliable photometry in a given band, set to "True" for sources that meet the quality criteria outlined in Section 2.3.4, and "False" for those that do not. A source marked with a True in any band is considered likely to be a star with well-measured photometry in this band, though it may still have False flags in other bands, signifying unreliable measurements in those bands. Sources flagged with False in all bands are deemed unlikely to be reliable photometry. The comprehensive catalog, which is 19 GB in size, is accessible at MAST as part of a HLSP via DOI:10.17909/aa43-mt38. This extensive catalog includes the combined measurements of each star across all bands, along with individual measurements from each exposure within the survey. We also provide catalogs for each brick individually to simplify downloads for studies interested in smaller sections of the disk.

3.2. Color–Magnitude Diagrams

The results of the culling process as illustrated in Section 2.3.4 are presented in the optical CMDs in Figure 10. These plots show the output ST catalog photometry for the entire survey in the optical bands, and label the most distinct features. The left panel shows all photometry measurements in the ST catalog, and the right panel shows the measurements that fail our GST quality criteria in both bands. The majority of the failed measurements are located at the faint end, where spurious and blended measurements are much more likely near the detection limit, while the few brighter ones are most likely contaminants and artifacts. The CMD overview comparison shows the high fidelity of the photometry for stars that pass our criteria metrics, which produces distinct, well-populated CMD features, while the stars that are excluded form a relatively featureless distribution. We further describe these features below.

The vertical narrow plume on the blue edge of the optical CMD shows the upper MS, which has a sharp blue edge as determined by the saturation of color when the stellar effective temperature ($T_{\rm eff}$) is hotter than $\sim 10^4$ K. The second less populated blue plume at color F475W − F814W ~ 1 shows the position of the BHeB sequence. This sequence records the

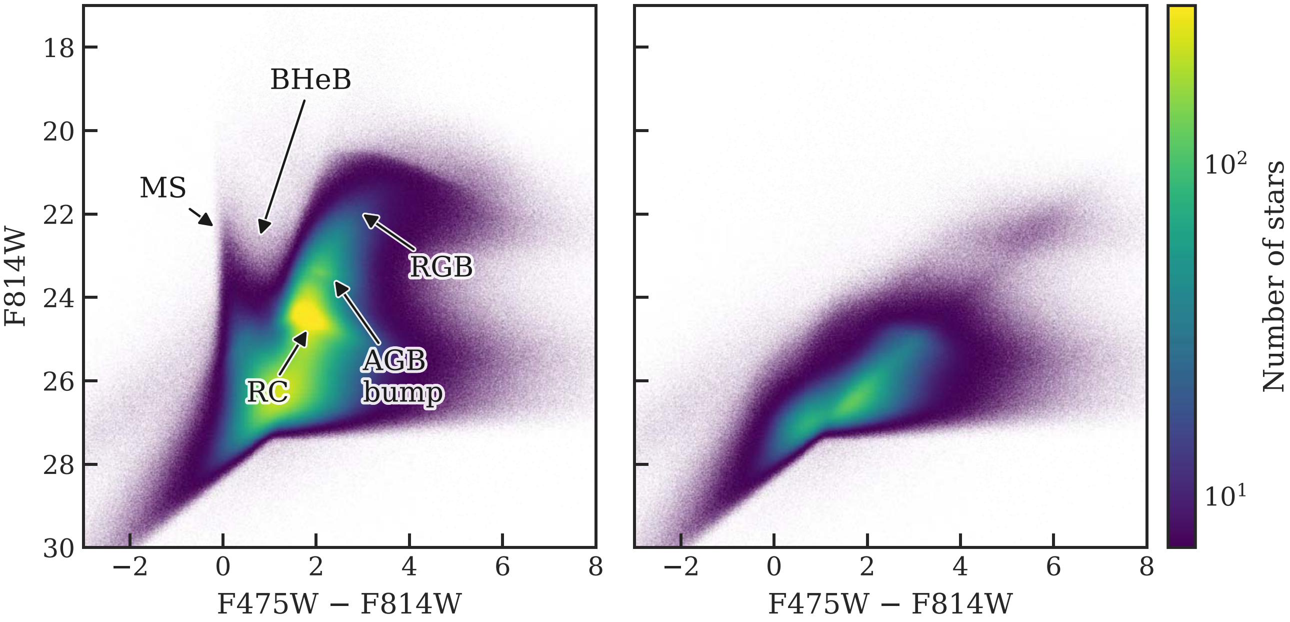

Figure 10. Left: optical (F475W − F814W) Hess diagram of the output ST catalog photometry for the entire survey. Typical CMD features are labeled: main sequence (MS), blue helium-burning (BHeB) sequence, RGB, asymptotic giant branch (AGB) bump, and RC. Right: same as left, showing measurements that fail our GST quality criteria in both optical bands. The failing measurements do not tend to mark these CMD features as labeled on the left, suggesting they are not reliable for population work.

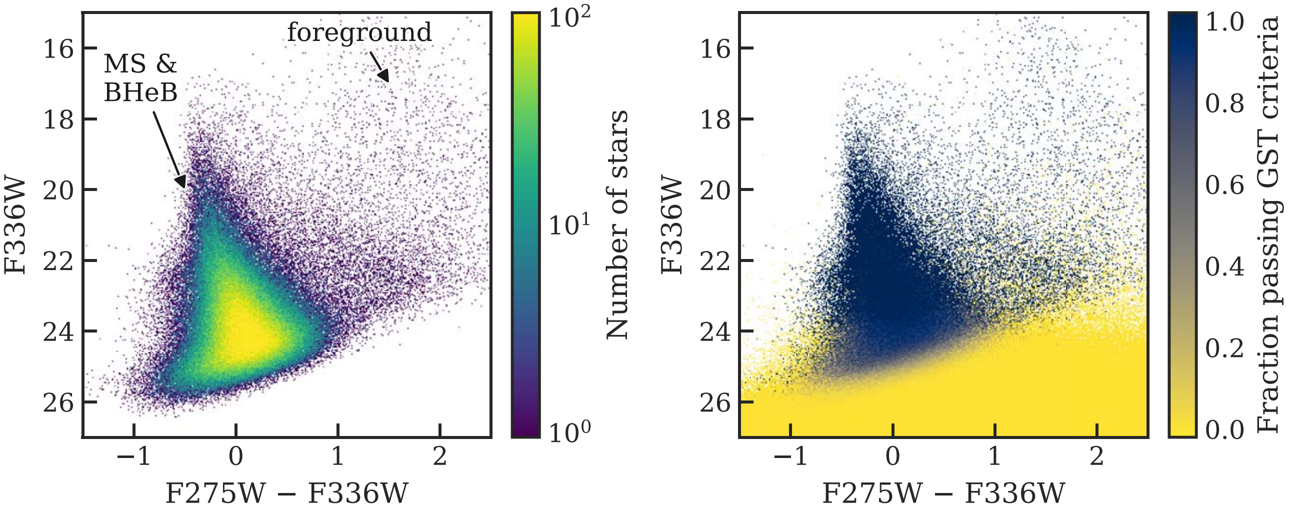

Figure 11. UV CMD for all F275W and F336W measurements in the entire survey. Left: CMD showing only measurements that pass our GST quality cuts in both bands. The GST quality criteria retain a high fraction of stars within the CMD features and a very low fraction of stars outside of these features. For a detailed distribution of foreground stars predicted by the `Trilegal` Galactic model for the survey region, see Figure 15. Right: fraction of accepted measurements flagged as passing our GST quality cuts in either of the two bands.

bluest stage for intermediate- and high-mass stars which go through the core-helium-burning phase. The sequences of MS and BHeB are both indicative of recent star formation, suggesting that M31 has been forming stars for hundreds of megayears. The red bright plume (F814W ∼ 21–23) marks the RGB, which shows evolved shell-hydrogen-burning low-mass stars. The tip of the red giant branch (TRGB) appears as a distinct edge at the bright end of the RGB (F814W ∼ 20.5), representing the point at which low-mass stars reach a critical luminosity before undergoing the helium flash and transitioning to the horizontal branch phase. Above and slightly to the right of the RGB in the CMD (F814W ∼ 18–21) lies the position of the AGB. The AGB phase represents the low- to intermediate-mass stars that have exhausted the hydrogen in their cores and are burning helium in a shell. This stage is characterized by significant changes in luminosity and color due to thermal pulses and extensive mass loss. Below this region, the AGB bump (F814W ∼ 23.5) records the early AGB stars, which undergo a pause in evolution when forming their double-shell structure (C. Gallart 1998). The prominent RC (F814W ∼ 24–25) shows the stable core-helium-burning low-mass stars. See Section 4.1 for stellar density maps with these distinct CMD features.

The CMDs in all bands for stars that meet our GST quality criteria, along with the fraction of accepted measurements over the same CMD space, are presented in Figures 11 and 12. Our GST quality cuts keep a very high fraction of the stars in these CMD features and a very low fraction of stars outside of these

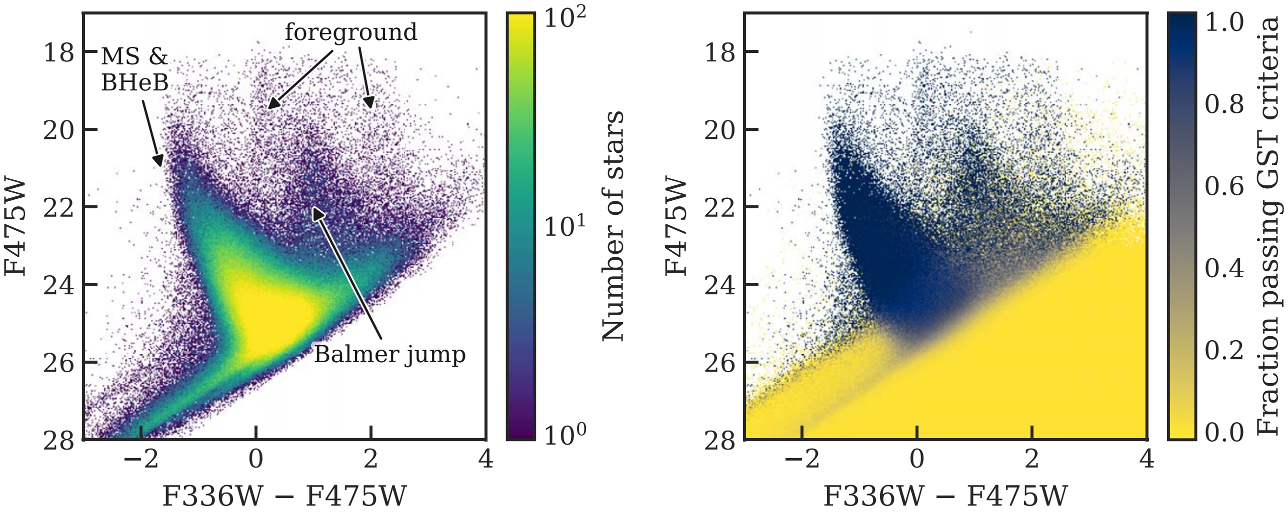

Figure 12. Same as Figure 11, showing F336W and F475W measurements. The vertical feature at F336W − F475W ∼ 0.8 is associated with the Balmer jump at 3646 Å. This phenomenon is characterized by a sudden increase in opacity due to the ionization of hydrogen atoms, resulting in stars with a relatively broad range of temperatures ($3.7 < \log(T_{\mathrm{eff}}) < 3.9$) having a common color in these bands. Additionally, note that the double boundary on the faint end (lower left) of the CMD reflects the different depths between the ACS/WFC and WFC3/UVIS. Due to the overlap structure, where there is less overlap in a small part of the survey, the data are shallower.

features. In Figure 13, the optical measurements in F475W and F814W are further divided by stellar density to show the effects of crowding across the disk. The stellar density range included in each CMD panel corresponds to the density maps illustrated in Figure 6. The density is calculated by the star counts with $21.5 < \mathrm{F814W} < 23$ arcsec^{-2} (see Section 2.3.5), which is also a proxy of galactocentric distance (except for the crowded regions near M32), as the stellar density falls off smoothly with radius. The optical bands are strongly affected by crowding, as apparent by the brighter magnitude limit at the higher stellar densities. See Section 3.4.1 for further quantitative analysis of the crowding effects from ASTs.

In general, the highest impact of any metric on the culling of the data is that of the S/N, which culls 100% of the measurements fainter than the detection limit in each band. We note that these quality cuts were chosen to produce high-quality CMDs from our catalogs over the entire survey, and may not be optimal for a specific analysis region or application. To prevent the exclusion of significant individual detections that failed to yield high-quality PSF fits, we have included all measurements that meet the ST criteria in at least one band in our final catalog. Additionally, a flag column is added to each band to indicate whether the measurement meets the GST criteria. Individuals utilizing our photometry for specific projects will likely prefer to establish their own flags, optimized to meet the requirements of their scientific objectives.

Figure 14 further illustrates the impact of depth in each band on the recovery of various CMD features. We presented the UV and optical CMDs of GST measurements in three density bins of the survey, color coded according to the median number of bands in which they were detected and passed the GST criteria. This visualization clearly shows that the UV observations are our shallowest, as nearly every UV detection also appears in all the other two optical bands, with no RGB stars detected in the UV. Conversely, almost every star in the catalog is detected in the optical bands, highlighting the deepest optical observations.

3.3. Foreground Contamination

Our photometry catalog of M31 has a small amount of contamination from Milky Way foreground stars. We estimate the level of the foreground contamination by producing model Galactic populations using the `Trilegal` software package. We use the default parameters in the `Trilegal` web interface[23] (L. Girardi et al. 2012), which are slightly modified from the original settings used in L. Girardi et al. (2005). These adjustments aim to better reproduce star counts in the Sloan Digital Sky Survey and Two Micron All-Sky Survey across the sky. This model suggests ∼5900 foreground stars in the entire PHAST survey footprint of ∼0.45 deg^2, with ∼2780 stars having $\mathrm{F336W} < 27$, and ∼5600 stars having $\mathrm{F475W} < 28$. Our catalog of over 90 million stars contains only <0.007% foreground contamination. This fraction only increases to <0.009% for the 70 million stars that pass our quality cuts in at least two bands. Although the foreground contamination is extremely low in the entire catalog, the features of these stars in the CMDs are still very evident to be identified from M31 populations. Figure 15 shows the CMDs of the foreground stars predicted by the Galactic model for our entire PHAST region at the depth of our survey, overlaid on the survey GST CMDs. The foreground stars draw nearly vertical sequences at colors $1 < \mathrm{F275W} - \mathrm{F336W} < 3$, $0 < \mathrm{F336W} - \mathrm{F475W} < 2$, and $1 < \mathrm{F475W} - \mathrm{F814W} < 4$. For the most part, the foreground occupies the space near the BHeB, along with slightly contaminating the RGB and AGB.

3.4. Artificial Star Test Results

For the AST results, we report a catalog with the AST inputs and a selection of output columns, including the location, input magnitude, difference between the recovered and input magnitudes (“Out-in”), output S/N, and output GST quality flag for each artificial star in each filter. An example of this summary can be seen in Table 4.

---

[23] http://stev.oapd.inaf.it/cgi-bin/trilegal_1.6

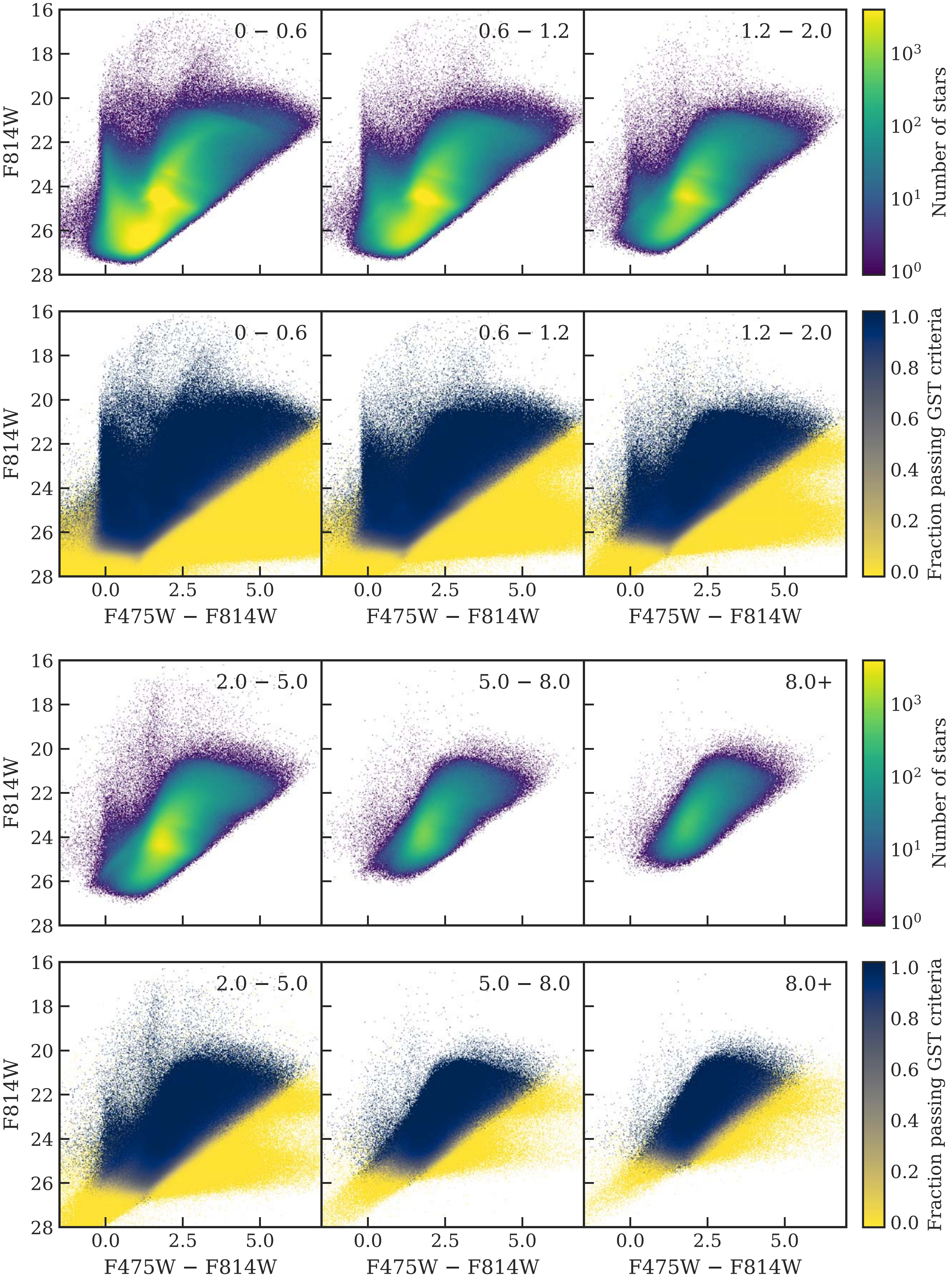

Figure 13. CMDs for all F475W and F814W measurements. The measurements are further divided by stellar density to show the crowding effects across the disk. The stellar density range labeled in each panel, in units of stars arcsec^{-2}, corresponds to the density map in Figure 6, where density is calculated based on star counts with $21.5 < \mathrm{F814W} < 23$ arcsec^{-2}. The optical bands are strongly affected by crowding, as apparent by the brighter magnitude limit at the higher stellar densities. Note that the vertical feature ($1.3 < \mathrm{F475W} - \mathrm{F814W} < 1.8$) observed in the density bin of 2.0–5.0 stars arcsec^{-2} is a crowding artifact, which can be removed by applying a strict crowding cut, such as `crowding` < 0.5 in both bands.

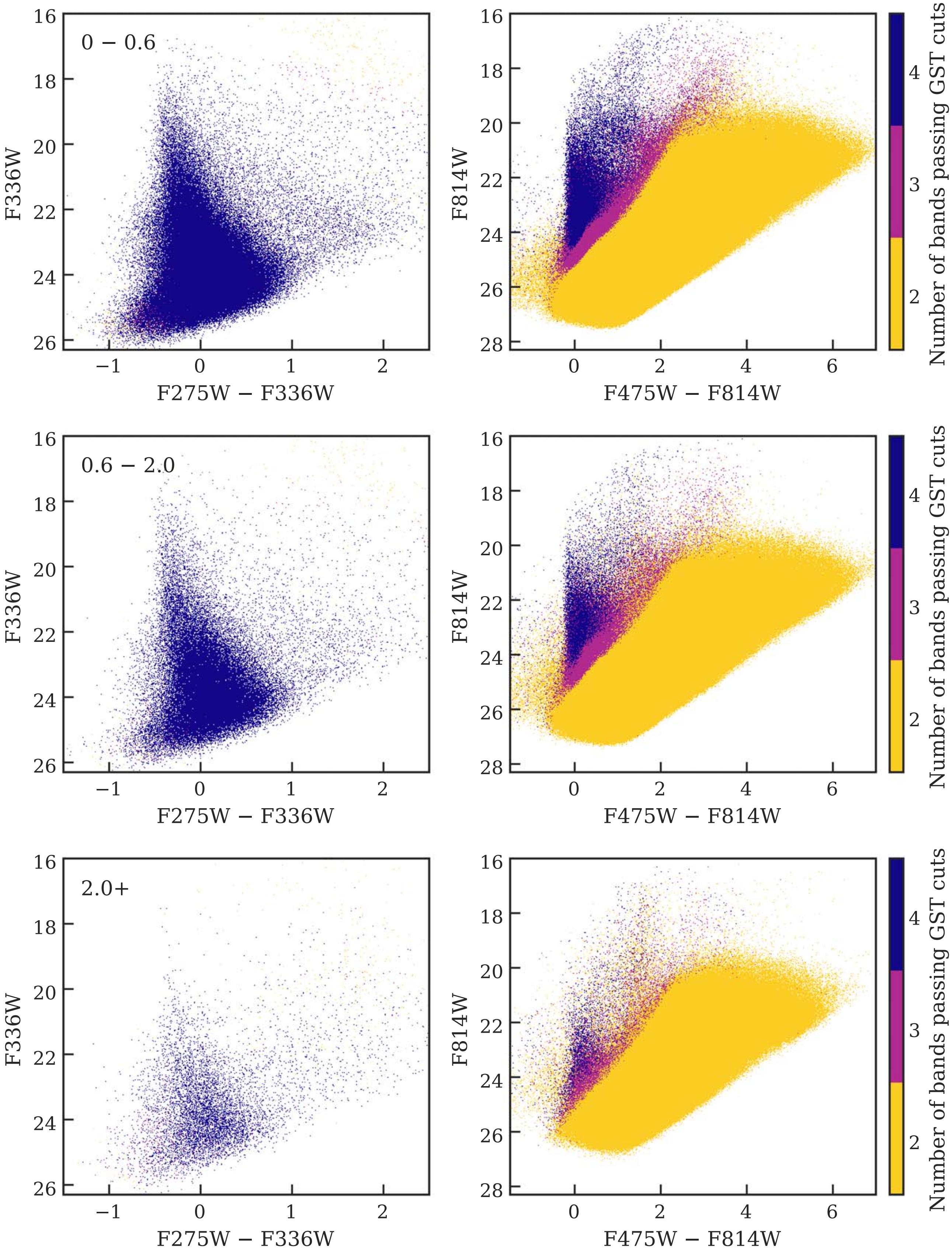

Figure 14. UV (left) and optical (right) CMDs of GST measurements in three density bins of the survey, representing low (top row), medium (middle row), and high (bottom row) stellar density regions, as labeled in units of stars arcsec^{-2}. Density is calculated by star counts with $21.5 < \mathrm{F814W} < 23$ arcsec^{-2}. The CMDs are color coded in the median number of bands in which a star passes the GST criteria. Nearly every detection in the NUV is detected in all four bands. Most RGB and AGB stars are only detected in two optical bands, highlighting the depth of the ACS data.

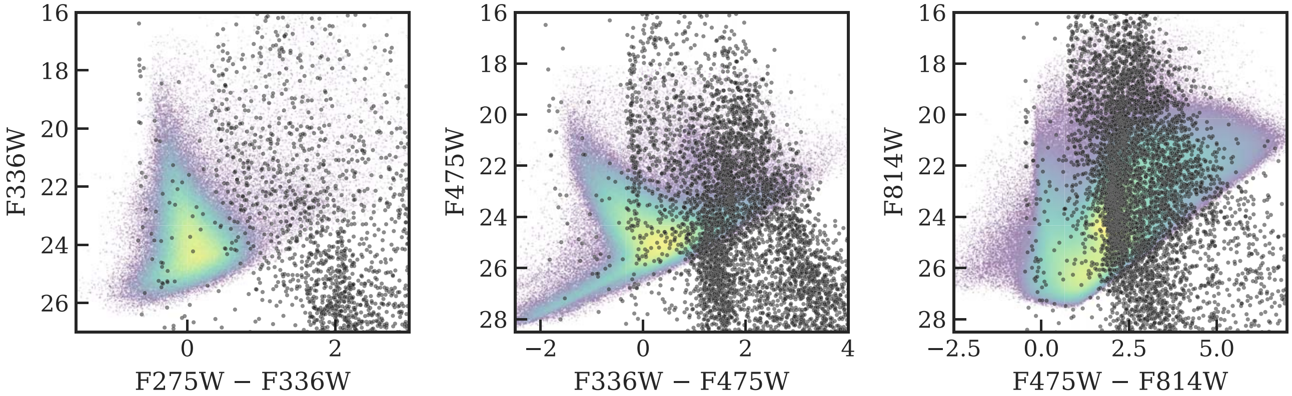

Figure 15. CMDs for the ∼5900 foreground stars (black scatter points) predicted by the `Trilegal` Galactic model for our overall ∼0.45 deg^2 PHAST region on the sky at the depth of our survey, overlaid on the GST CMDs. The foreground stars draw nearly vertical sequences at colors $1 < \mathrm{F275W} - \mathrm{F336W} < 3$, $0 < \mathrm{F336W} - \mathrm{F475W} < 2$, and $1 < \mathrm{F475W} - \mathrm{F814W} < 4$. While the foreground stars make up <0.007% of the entire catalog, these sequences are still evident in the less well-populated regions of the observed CMDs.

3.4.1. Data Quality

The DQ of the photometry catalog of the PHAST survey is further analyzed and evaluated via the ASTs as illustrated in Section 2.4. We calculated the magnitude m_{50} at which 50% of the inserted artificial stars are recovered. We present this “50% completeness limit” in each filter as a function of stellar density in Figure 16 and Table 5. Generally, this limit is largely determined by the number of photons detected from an astronomical source. However, in areas of high stellar density, this completeness limit is restricted by the magnitude at which the high surface density sources would invariably blend with brighter sources, making the original source indiscernible. Thus, the majority of observations in the optical for our PHAST survey are “crowding limited” rather than “photon limited;” that is, the limiting magnitude is more significantly affected by stellar density than by photon-counting statistics.

In the UV, our images do not experience significant crowding, as they do not reach the magnitudes where UV-detectable stars become numerous. The UV observations achieve a depth of $\mathrm{F275W} \sim 24.8$ mag, which remains relatively consistent across different stellar densities throughout the disk, indicative of photon-limited images. In contrast, the depth of optical observations varies by more than 2 mag from the inner regions of PHAST to the outer regions, demonstrating the influence of stellar crowding. Figure 17 illustrates the distinct completeness patterns between photon-limited and crowding-limited observations. In photon-limited data, such as the F275W and F336W in the UV, completeness sharply declines from nearly 100%–0% within a span of ∼1 mag. Conversely, in crowding-limited data, completeness decreases more gradually over a broader magnitude range, exceeding 3 mag. This gradual decrease in completeness is partly due to the increased probability of a star failing the quality checks as the likelihood of it blending with another star of similar brightness increases.

Our photometry underwent further evaluations using the rms uncertainties and median magnitude bias derived from the ASTs, along with the corresponding error reported by DOLPHOT. We also examined the ratio of the rms uncertainty to the DOLPHOT-reported error across various stellar densities, filters, and magnitudes. Table 6 includes all numerical measurements of bias and uncertainty for the different filters and levels of source density. Figure 18 presents the rms scatter of the median difference between the recovered and input magnitudes as a function of input magnitude for each band, along with the 16th and 84th percentile ranges for the distribution of differences, all plotted across a range of mean local densities. Positive values indicate sources that are recovered at fainter magnitudes than their true magnitudes.

The magnitude biases and photometric uncertainties arise from a combination of photon-counting errors and the effects of crowding. These effects include uncertainties and biases associated with the deblending of neighboring sources, sky estimation inaccuracies, and brightward biases due to blending with undetected sources. The observed scatter uncertainty between the true and recovered magnitudes is typically about 20% larger than the photon-counting uncertainty (as quantified by DOLPHOT) in UV observations, and ∼4 times greater in optical observations. Both the bias and measurement uncertainties increase at fainter magnitudes, where the challenges of photon counting and crowding intensify. Generally, the biases are 2–4 times smaller than the photometric uncertainties.

In optical observations, biases and uncertainties increase in areas with higher source densities due to more pronounced crowding effects. In less dense regions of the survey with stellar density lower than 1.2 stars arcsec^{-2}, which constitute the majority of our survey, the magnitude bias is less than 0.1 above the photometry depth. However, in the denser regions of the survey, the sources that are intrinsically fainter would be measured toward brighter magnitudes as a result of unresolved, overlapping sources elevating the brightness of the inserted artificial stars above the detection threshold. This crowding bias is particularly concerning in the densest parts of the the M31 bulge (Brick 25), where it begins to impact photometry near the TRGB in the F814W filter. Consequently, in the survey’s most crowded regions, this bias can lead to RGB stars being measured as brighter than the TRGB.

In the UV, we observe an increase in bias and uncertainty for fainter sources, a trend that is largely independent of the local source density due to the absence of significant crowding issues in the UV. Across all survey areas, the UV photometry exhibits a bias that goes from approximately 0 mag at the bright end to ∼0.1 mag at the faint end. Similarly, uncertainties range from ∼0.01 mag for brighter sources to ∼0.2 mag for fainter ones. Notably, the bias in the UV starts to become significant toward the fainter end, contrasting with the trend observed in the optical measurements. This phenomenon, also noted in the

Table 4
Sample Artificial Star Data

R.A. (J2000)	Decl. (J2000)	F275W (input)	Out-in	S/N	GST	F336W (input)	Out-in	S/N	GST	F475W (input)	Out-in	S/N	GST	F814W (input)	Out-in	S/N	GST
10.561444	41.218254	36.126	63.873	0.0	F	34.560	65.439	0.0	F	32.735	−6.955	12.0	T	29.892	−5.850	13.3	T
10.561482	41.218229	23.580	0.071	5.1	T	20.664	−0.018	39.6	T	18.306	−0.005	841.8	T	15.900	84.099	0.0	F
10.561532	41.218109	30.971	69.028	0.0	F	30.313	69.686	0.0	F	30.052	69.947	0.0	F	28.849	71.150	0.0	F
10.561601	41.218101	14.055	−0.006	923.3	T	14.183	−0.005	812.8	T	15.286	84.713	0.0	F	14.984	85.015	0.0	F
10.561610	41.218195	23.615	0.199	6.3	T	21.965	0.132	12.6	T	21.220	0.000	353.7	T	20.150	0.005	348.3	T
10.561664	41.217965	20.574	0.045	43.4	T	19.991	−0.029	55.1	T	19.945	0.000	613.4	T	18.748	0.009	745.6	T
10.561688	41.217981	34.894	65.105	0.0	F	33.396	66.603	0.0	F	31.737	68.262	0.0	F	27.553	72.446	0.0	F
10.561706	41.218114	37.754	62.245	0.0	F	36.129	63.870	0.0	F	32.599	−7.446	24.7	T	27.556	−3.927	14.7	T
10.561719	41.217766	23.378	−0.009	6.7	T	22.660	0.031	12.8	T	21.549	0.006	292.5	T	20.666	−0.003	268.5	T
10.561732	41.218261	10.813	89.186	0.0	F	11.408	88.591	0.0	F	13.040	86.959	0.0	F	13.413	86.586	0.0	F

(This table is available in its entirety in machine-readable form in the online article.)

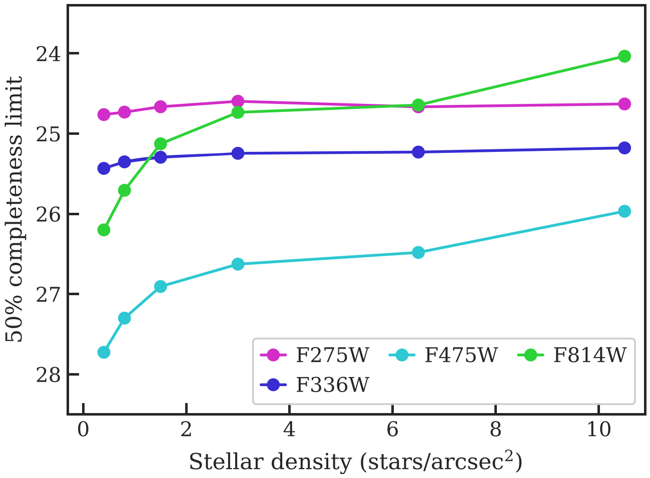

Figure 16. Magnitudes at which we measure 50% completeness by stellar density in four filters. Stellar density range corresponds to the density maps shown in Figure 6, where density is calculated by the star counts with $21.5 < \mathrm{F814W} < 23$ arcsec^{-2}. Each density scatter point represents the median density in this bin. Completeness limits in the UV are largely consistent over the full density range of the survey, whereas they grow brighter with increasing density in the optical due to crowding.

Table 5
50% Completeness Limits by Stellar Density

Stellar Density	F275W	F336W	F475W	F814W
0–0.6	24.76	25.43	27.73	26.20
0.6–1.2	24.73	25.35	27.30	25.71
1.2–2.0	24.67	25.30	26.91	25.13
2.0–5.0	24.60	25.25	26.63	24.74
5.0–8.0	24.67	25.23	26.48	24.64
8.0+	24.63	25.18	25.97	24.04

Note. Stellar density is calculated by the star counts with $21.5 < \mathrm{F814W} < 23$ arcsec^{-2}.

PHAT and PHATTER surveys, may be attributed to a slightly elevated background measurement inherent to our technique.

3.5. Luminosity Functions

Quantitative tests were performed on the fidelity and consistency of standard CMD features in order to assess the robustness and homogeneity of our photometry catalog. Both the TRGB and RC are prominent features well suited to the quantitative quality checks. We compared the locations of these features in the luminosity functions across different fields of the entire survey. The left panel in Figure 19 displays the selection regions for the TRGB and the RC on the optical CMD of the entire survey.

To examine the TRGB feature, we selected stars in the color range $3.0 < \mathrm{F475W} - \mathrm{F814W} < 3.5$ at $\mathrm{F814W} = 20.5$ and $20.1 < \mathrm{F814W} < 21.1$ in regions of the survey with stellar density lower than 2 stars arcsec^{-2} (to avoid crowding bias), where density is calculated by the star counts with $21.5 < \mathrm{F814W} < 23$ arcsec^{-2}. The normalized F814W luminosity function (upper right panel) shows the exceptional consistency of the photometry across the survey. The luminosity function steepens at the TRGB, where the apparent TRGB magnitude is consistent within the uncertainties with the predicted $m_{\mathrm{TRGB}} = 20.52 \pm 0.1$ using $M^{I}_{\mathrm{TRGB}} = -4.05 \pm 0.1$ (R. L. Beaton et al. 2018), assuming a typical M31 foreground extinction A_{F814W} of 0.17 (E. F. Schlafly & D. P. Finkbeiner 2011) and a distance modulus of $m - M = 24.47$ (A. W. McConnachie et al. 2005). Our absolute photometric calibration is accurate and the amount of systematic uncertainty over large areas of the catalog is small.

Additionally, we examined the position of the well-populated RC feature, selecting stars within $1.5 < \mathrm{F475W} - \mathrm{F814W} < 2.2$ at $\mathrm{F814W} = 24.39$ and $23.8 < \mathrm{F814W} < 25.0$ in survey regions where the stellar density is lower than 2 stars arcsec^{-2}. The normalized luminosity function in F814W (lower right panel) is compared to the center of the RC feature $m_{\mathrm{RC}} = 24.39 \pm 0.05$ estimated from the PHAT survey (B. F. Williams et al. 2014). A direct comparison of the RC centers shows that the RC in the PHAST data appears to be fainter by ∼0.05 mag in F814W.

We tested the possibility that the difference in RC peak magnitude could be related to some systematic bias between the PHAT and PHAST photometry by matching stars measured in both surveys in the overlapping region and comparing their photometry. We find that the photometry difference between the PHAT and PHAST around the RC magnitude is consistent to better than 2%. A Gaussian fit to the residuals in the photometry between the matched stars near the RC has a peak at $\Delta\mathrm{F814W}_{\mathrm{PHAST-PHAT}} \sim -0.017$ mag and a width of 0.14 mag. Considering this consistency, the RC feature in the southern disk from the PHAST survey is apparently fainter in general than the RC feature in the northern disk, possibly due to differences in the reddening distribution or in the stellar populations, as the RC feature shifts in brightness and color with age and metallicity. Older, more metal-rich stars appear at fainter and redder positions on the model CMDs (e.g., B. F. Williams et al. 2009b). We will be further examining and quantifying such differences in future work.

3.6. Stellar Photometric Spectral Energy Distribution Fitting

The BEAST (K. D. Gordon et al. 2016) offers a probabilistic approach to modeling the dust-extinguished photometry SED of an individual star, accounting for observational uncertainties. The BEAST is designed to infer the physical properties of individual stellar sources from a set of photometric measurements, incorporating an observational uncertainty model and assuming stellar evolution and atmosphere models. This tool has been specifically formulated for use with large multiband surveys of resolved stellar populations in the Local Group, and it has demonstrated its accuracy and precision with the application to the PHAT six-band photometry catalog of M31 (K. D. Gordon et al. 2016) and other nearby galaxies (e.g., Y. Choi et al. 2020).

The accuracy of measurements from the BEAST depends on the wavelength range of the measured SED. Figure 20 shows the accuracy of the stellar and dust parameters recovered from different combinations of filters. While PHAT had observations spanning the NUV, optical, and IR, we have found that our four NUV and optical bandpasses provide sufficient wavelength coverage to constrain the properties of most stars in our survey, enabling constraints on parameters such as T_{eff}, M_{initial}, and A_V, and estimates of stellar age. Fits to the models indicate that the recovery is less reliable for highly extincted stars ($A_V \gtrsim 4$). Our depth and filter combination are not particularly sensitive to

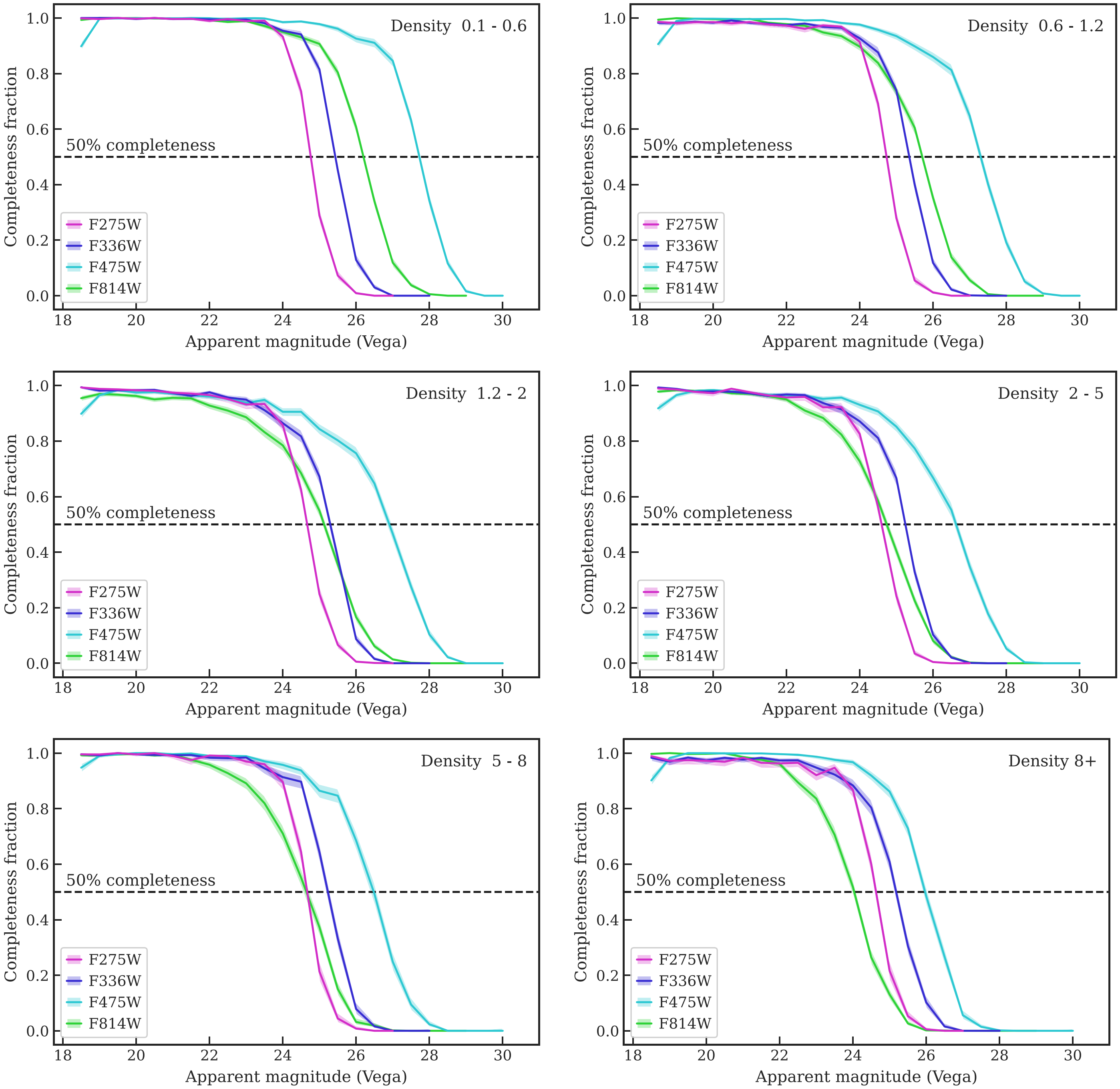

Figure 17. Photometric completeness (fraction of input stars that pass quality cuts) as a function of input magnitude in all filters for six characteristic density bins (labeled in the upper right corners, where density is calculated by the star counts with $21.5 < \mathrm{F814W} < 23$ arcsec^{-2}). Shaded regions show 95% confidence using the Jeffreys interval.

such highly extincted populations, partially because we do not include the IR bands. Thus, when fitting the PHAST data, the range should be limited to $A_V < 4$.

In Figure 21 we show and describe an example of a BEAST SED fit and resulting star and dust parameters for a single source in PHAST Brick 28. This fit is for a typical star with detections in all four bands. The contributions of the components of the SED of the best-fitting model (stellar, dust, and photometric bias) are shown in the left panel illustrating the impact of dust and photometric measurement bias on the observed flux. The right side shows the resulting values and errors of the star and dust parameters derived from the fit.

Thus, results from the BEAST have further demonstrated the value of our catalog for studying individually well-measured stars, as well as for conducting statistical studies that take advantage of the large number of sources detected in modern surveys. One example of the application of BEAST fittings on large number of sources is the investigation of an “[O III] burst” near M31’s disk, discovered by amateur astronomers (M. Drechsler et al. 2023), from the point of view of nearby stars. This feature appears to be an outflow from M31’s 10 kpc ring

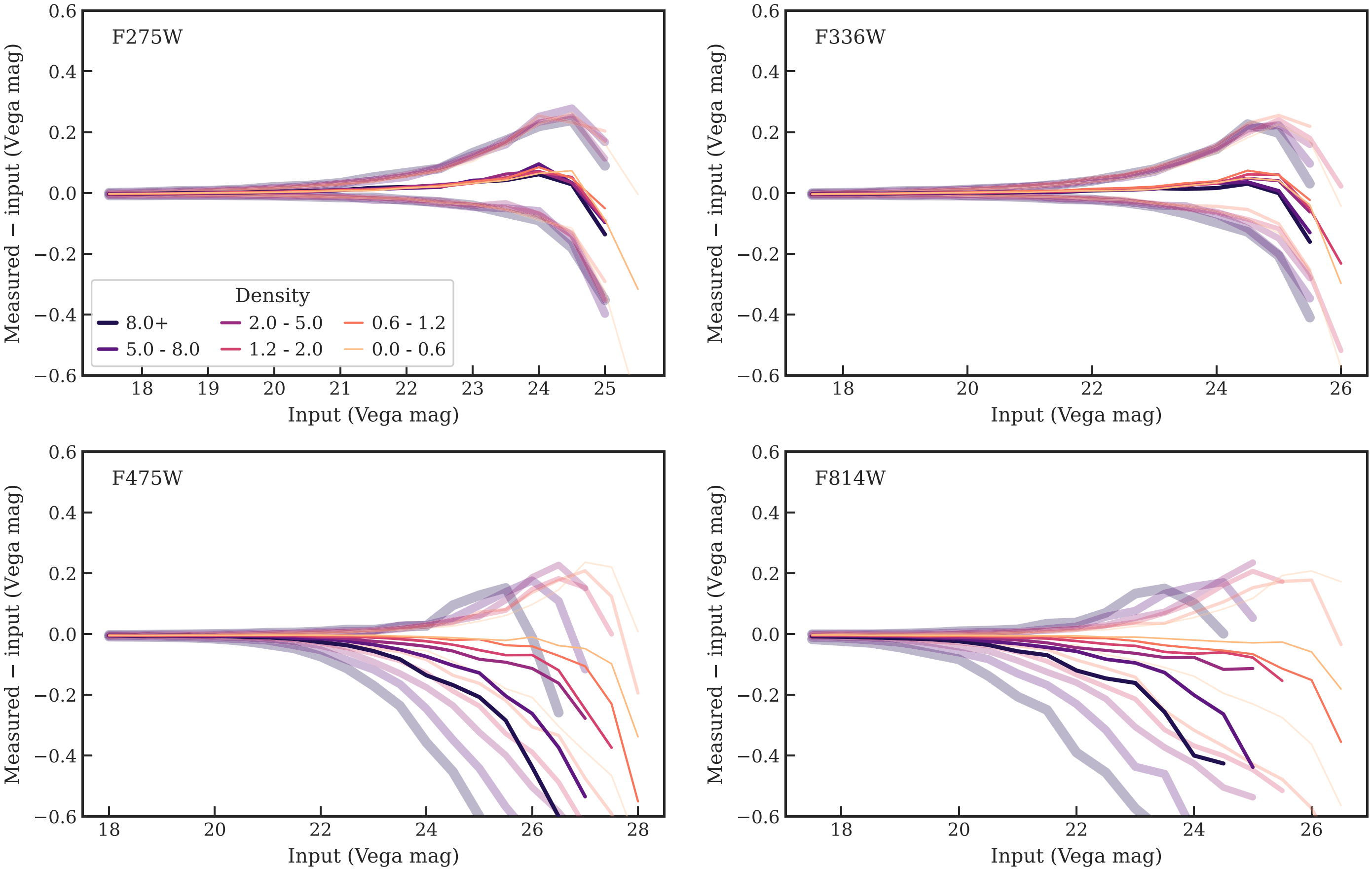

Figure 18. Photometric bias (thin solid lines) and $\pm 1\sigma$ uncertainty ranges (thick faded lines) derived from ASTs as a function of input magnitude in each filter for six density bins, where density is calculated by the star counts with $21.5 < \mathrm{F814W} < 23$ arcsec^{-2}. The bias is taken to be the median of the measured minus input AST magnitudes in 0.5 mag bins, and the uncertainty bounds are the 16th and 84th percentiles of the same. Darker line colors correspond to higher densities.

Table 6

Sample Photometric Bias, Artificial Star Test–derived Uncertainty, DOLPHOT-reported Uncertainty, Artificial Star Test/DOLPHOT Uncertainty Ratio, and Stellar Density

Density	Filter	Magnitude	Bias	Uncertainty	DOLPHOT	Ratio
8.0+	F275W	17.5	−0.003874	0.004043	0.003988	1.013816
8.0+	F275W	18.0	−0.002989	0.004946	0.004977	0.993748
8.0+	F275W	18.5	−0.000977	0.006548	0.005975	1.095970
8.0+	F275W	19.0	0.000082	0.007130	0.007008	1.017510
8.0+	F275W	19.5	0.001016	0.009488	0.008989	1.055468
8.0+	F275W	20.0	0.003984	0.014410	0.011991	1.201787
8.0+	F275W	20.5	0.005938	0.017952	0.014989	1.197661
8.0+	F275W	21.0	0.009191	0.023932	0.020978	1.140853
8.0+	F275W	21.5	0.017015	0.033492	0.026996	1.240647
8.0+	F275W	22.0	0.019502	0.045162	0.036979	1.221293
8.0+	F275W	22.5	0.023088	0.055259	0.049979	1.105645
8.0+	F275W	23.0	0.035904	0.086566	0.071989	1.202494
8.0+	F275W	23.5	0.041939	0.119316	0.100003	1.193126
8.0+	F275W	24.0	0.061184	0.154768	0.145985	1.060167
8.0+	F275W	24.5	0.028114	0.209920	0.195019	1.076409
8.0+	F275W	25.0	−0.136406	0.220976	0.227025	0.973356

Note. Stellar density is calculated by the star counts with $21.5 < \mathrm{F814W} < 23$ arcsec^{-2}.

(This table is available in its entirety in machine-readable form in the online article.)

toward M32. The BEAST SED fittings of ∼10,000 stars in this field revealed an age distribution peaking at ∼100 Myr (Z. Chen et al. 2024, in preparation). The modeled age and ionizing fluxes from these UV-bright stars will help further discern whether this outburst arises from photoionization or a shock from M32's passage, and will predict the relative direction of M32's proper motions to M31, identifying M32's role in M31's merger history.

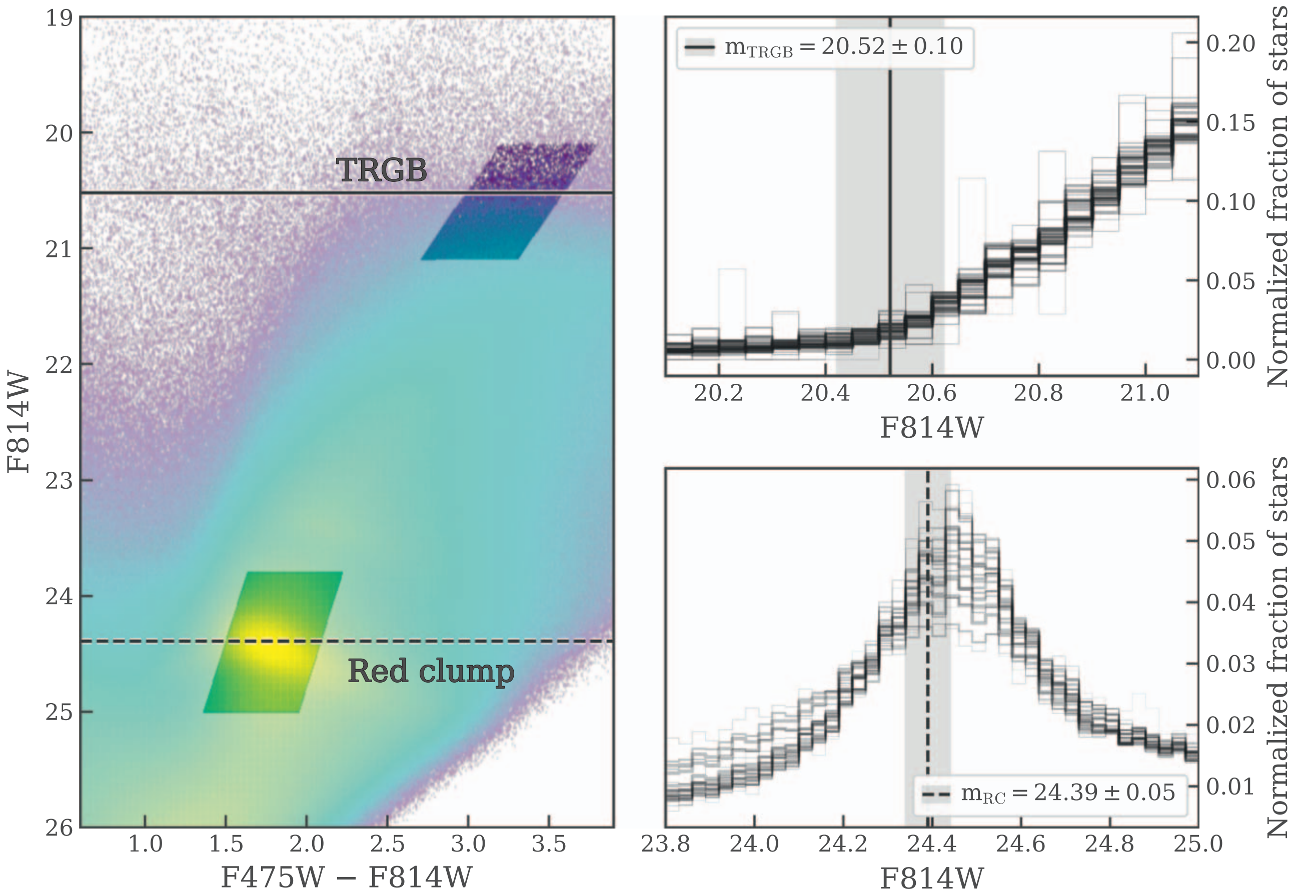

Figure 19. Left: optical CMD showing the selection regions used to measure the F814W luminosity functions for the TRGB and RC features. The solid line marks the predicted apparent TRGB magnitude using $M^{I}_{\mathrm{TRGB}} = -4.05$ (R. L. Beaton et al. 2018) with a distance modulus of $m - M = 24.47$ (A. W. McConnachie et al. 2005) and M31 foreground extinction of $A_V = 0.17$ (E. F. Schlafly & D. P. Finkbeiner 2011). The dashed line marks the center of the RC feature estimated from the PHAT survey (B. F. Williams et al. 2014). Right: normalized F814W luminosity functions for the TRGB (top) and RC (bottom) for survey regions with stellar density lower than 2 stars arcsec^{-2}, with each line weighted by the number of stars per sample. Vertical bands display the predicted TRGB $m_{\mathrm{TRGB}} = 20.52 \pm 0.1$ (top) and the center of RC from PHAT $m_{\mathrm{RC}} = 24.39 \pm 0.05$ (bottom). The TRGB magnitude distribution is consistent with the prediction across the entire survey. The RC peaks in the southern disk from the PHAST survey are slightly fainter than those observed in the northern half from PHAT. Given the photometry of matched PHAT and PHAST RC stars is consistent, with $\Delta\mathrm{F814W}_{\mathrm{PHAST-PHAT}} \sim -0.017$ in overlapping regions, the slightly fainter RC peaks in the southern disk hint at true differences in the stellar populations between the northern and southern regions.

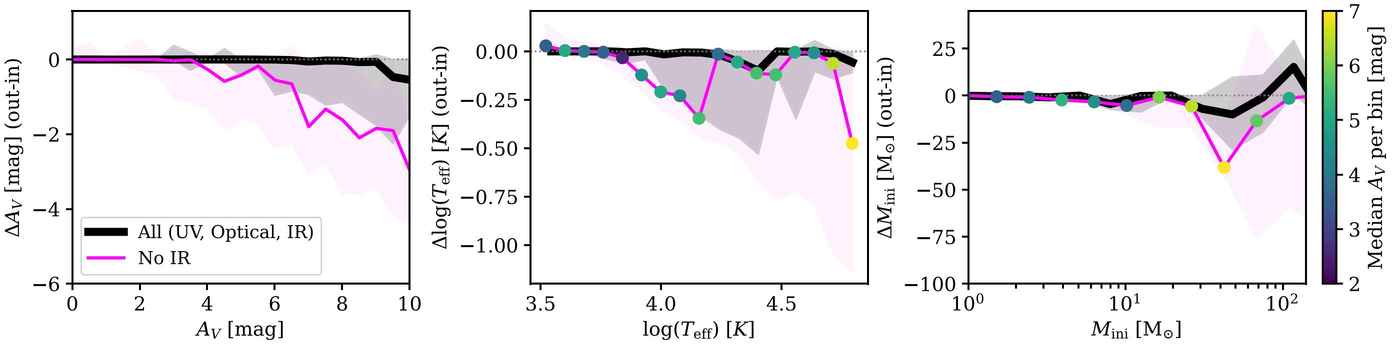

Figure 20. The accuracy of recovered stellar and dust parameters for different combinations of broadband filters, computed by performing SED fitting on artificially generated data, assuming photometric quality characteristic of the PHAT and PHAST observations. Left to right: median differences between the inferred and input A_V, T_{eff}, and M_{initial} for combinations with or without IR observations. In the right two panels, the curve without IR is further color coded by the median A_V per bin on the T_{eff} and M_{initial}, showing the impact of A_V on fitting the other parameters. The most discrepant recovery of parameters without IR observations corresponds to high A_V values. Combinations of UV and optical filters, reflective of those obtained in the PHAST survey, provide results comparable to the full UV + optical + IR set from the PHAT survey, except for the highest line-of-sight extinctions ($A_V \gtrsim 4$).

4. Discussion

4.1. Population Maps

We produced stellar density maps for populations with some of the most distinct features in the CMDs (also see Figure 10). Figure 22 illustrates the selection boundaries of the CMD used to select four approximate age groups: MS (young), helium burning (HeB; young), AGB (intermediate age), and RGB (old) populations. We follow selection boundaries from A. Smercina et al. (2023) for MS and HeB,

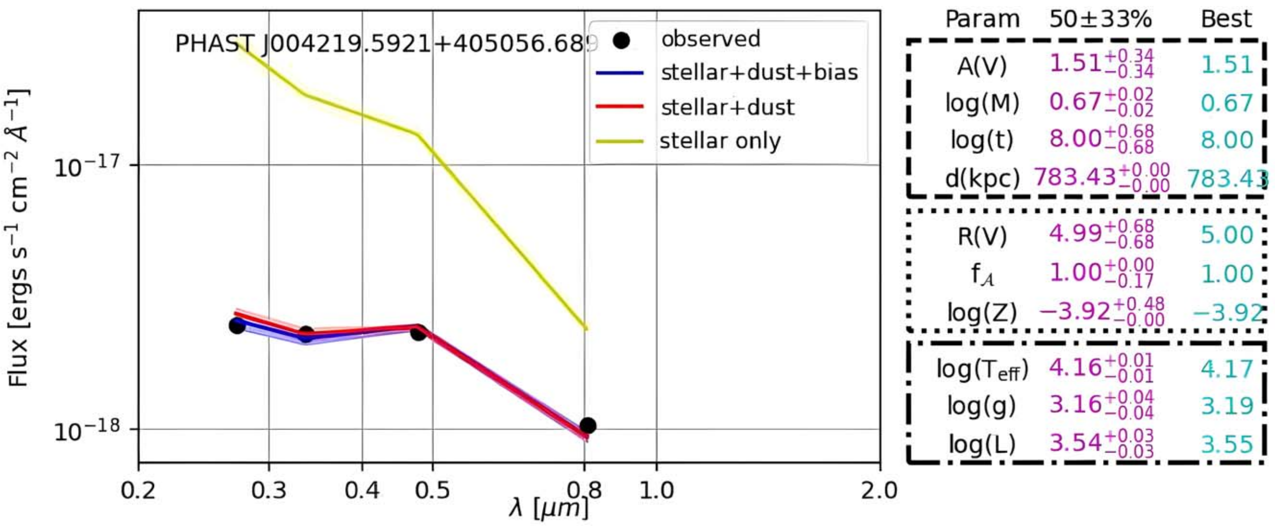

Param	50±33%	Best
A(V)	$1.51^{+0.34}_{-0.34}$	1.51
log(M)	$0.67^{+0.02}_{-0.02}$	0.67
log(t)	$8.00^{+0.68}_{-0.68}$	8.00
d(kpc)	$783.43^{+0.00}_{-0.00}$	783.43
R(V)	$4.99^{+0.68}_{-0.68}$	5.00
$f_{\mathcal{A}}$	$1.00^{+0.00}_{-0.17}$	1.00
log(Z)	$-3.92^{+0.48}_{-0.00}$	−3.92
log(T$_{\rm eff}$)	$4.16^{+0.01}_{-0.01}$	4.17
log(g)	$3.16^{+0.04}_{-0.04}$	3.19
log(L)	$3.54^{+0.03}_{-0.03}$	3.55

Figure 21. The fitting results for a typical star in Brick 28 with detections in all four bands. The 50% model is displayed, with shaded colored regions indicating the range of models that fit within 1σ. The models presented include the full model, which accounts for observational bias (stellar + dust + bias), the physical model alone (stellar + dust), and the stellar model alone (stellar). The best-fit values (cyan) and the 50% ± 33% values (magenta) of the star and dust parameters are presented numerically on the right side: extinction, A_V; star's initial mass, $\log(M)$; age, $\log(t)$; distance, d; extinction ratio parameter, $R(V)$; fraction of the $\mathcal{A}$-type extinction, $f_{\mathcal{A}}$ (see more in K. D. Gordon et al. 2016); metallicity, $\log(Z)$; effective temperature, $\log(T_{\rm eff})$; surface gravity, $\log(g)$; and luminosity, $\log(L)$.

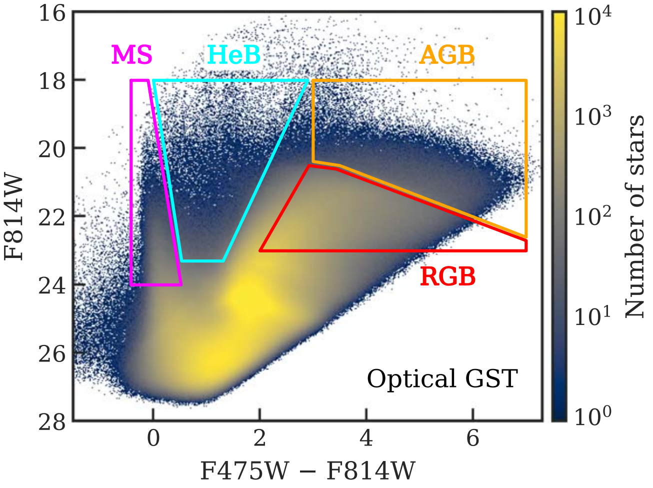

Figure 22. Optical CMD with GST stars showing selection regions for four stellar subpopulations of different characteristic ages. The outlines show the CMD regions from which the MS (magenta polygon), HeB (cyan polygon), AGB (orange polygon), and RGB (red polygon) populations were extracted. The limiting magnitude of the MS selection region roughly corresponds to $\gtrsim$80% completeness in the relevant bands. The MS probes ~3–200 Myr, and the HeB probes ~30–500 Myr. The AGB probes ~0.8–2 Gyr and the RGB probes $\gtrsim$2 Gyr.

and C. E. Dorman et al. (2015) for AGB and RGB. Figure 23 presents the density maps of each of these populations. The maps of the younger populations, identified through MS stars (aged 3–200 Myr) and HeB stars (aged 30–500 Myr), reveal pronounced spiral arm structures, whereas the older populations, traced by AGB stars (aged 0.8–2 Gyr) and RGB stars (aged over 2 Gyr), display a smoother density gradient typical of a disk galaxy.

Figure 24 further compares the maps of the younger populations of HeB and MS from PHAT and PHAST, with the Wide-field Infrared Survey Explorer (WISE; e.g., E. L. Wright et al. 2010) IR and GALEX UV (D. A. Thilker et al. 2005) images. The WISE image used all four bands at 3.4, 4.6, 12, and 22 μm (W1, W2, W3, and W4, respectively), capturing dust heated by young, massive stars in yellow/red and more mature stars in blue. By heavily weighting the W3 and W4 channels, this WISE image highlights emission from polycyclic aromatic hydrocarbons (PAHs), which are a significant component of the warm dust often found in star-forming regions.

The GALEX image combines both the FUV (shown as blue) and NUV (shown as yellow) bands. The FUV highlights the hottest, youngest, and most massive stars and star-forming regions, along with nearby ionized gas regions traced by Hα emission. The NUV captures light from slightly older and cooler stars, including hot post-AGB stars, which trace dense older populations such as the bulge, globular clusters, and M32, as well as foreground lower MS stars. It is noteworthy that the bulge exhibits significant brightness in the NUV due to the presence of evolved, likely metal-rich, old stars (P. Rosenfield et al. 2012). This characteristic accounts for its absence in the MS map.

The stellar density maps of the younger populations from our PHAT and PHAST surveys serve as direct tracers to quantify the spiral structure in the star-forming disk of M31. Our catalog allows us to map these structures across both sides of the disk using individual stars for the first time. The most prominent feature in these younger population maps is the bright, ~10 kpc radius ring of star formation (e.g., H. J. Habing et al. 1984; W. Rice 1993), as seen previously in many surveys (e.g., H. Arp 1964; N. A. Devereux et al. 1994; K. D. Gordon et al. 2006). Additionally, the split portion of the ring near the position of M32 (M. Haas et al. 1998), is seen to extend over roughly a quarter of the ring.

The morphology of M31's disk from our survey appears more disturbed on the southwestern side of the galaxy. The known interactions between M31 and its satellite galaxy M32 may help to explain the deviations from a regular spiral structure. Dynamical modeling of the interaction effects of M32 on M31 (K. D. Gordon et al. 2006) suggests that a passage of M32 through M31's disk ~20 Myr ago resulted in a burst of star formation that propagated outward through the

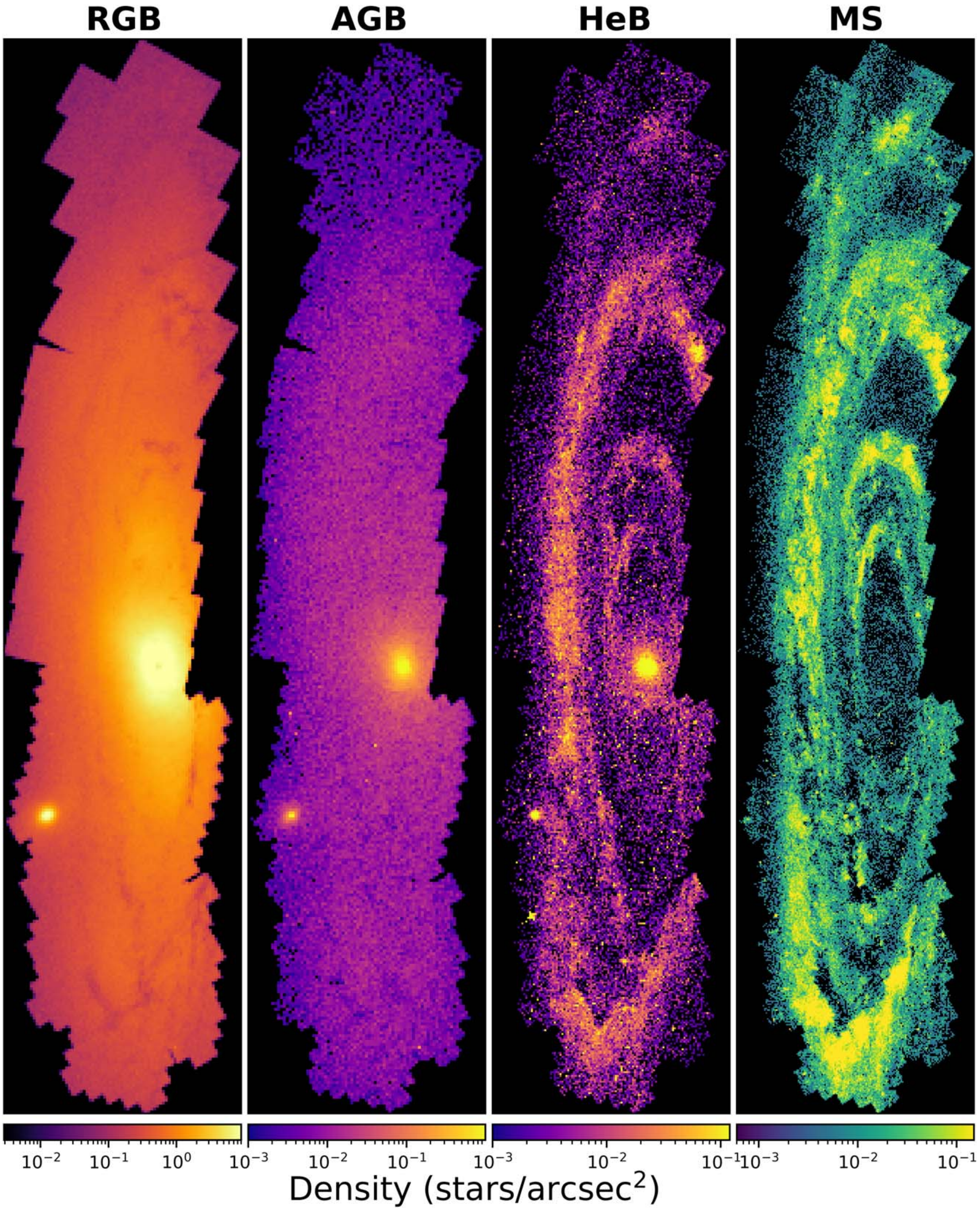

Figure 23. Stellar density maps of M31 (PHAT and PHAST) from four CMD features in Figure 22 that are proxies for subpopulations with different characteristic ages. The MS probes ∼3–200 Myr, and the HeB probes ∼30–500 Myr. The AGB probes ∼0.8–2 Gyr and the RGB probes $\gtrsim$2 Gyr. The two younger populations are more highly structured than the two older populations.

disk, creating a large hole similar in size and location to the observed splitting of the star-forming ring as seen from the IR-emitting structure. The stellar density maps from our PHAT and PHAST surveys reveal a consistent morphology, and the resolved photometry should allow us to probe the ages of the stars in these structures and trace their formation and evolution, as in A. R. Lewis et al. (2015, 2017). These maps support the idea that M31 has been distorted by interactions with its

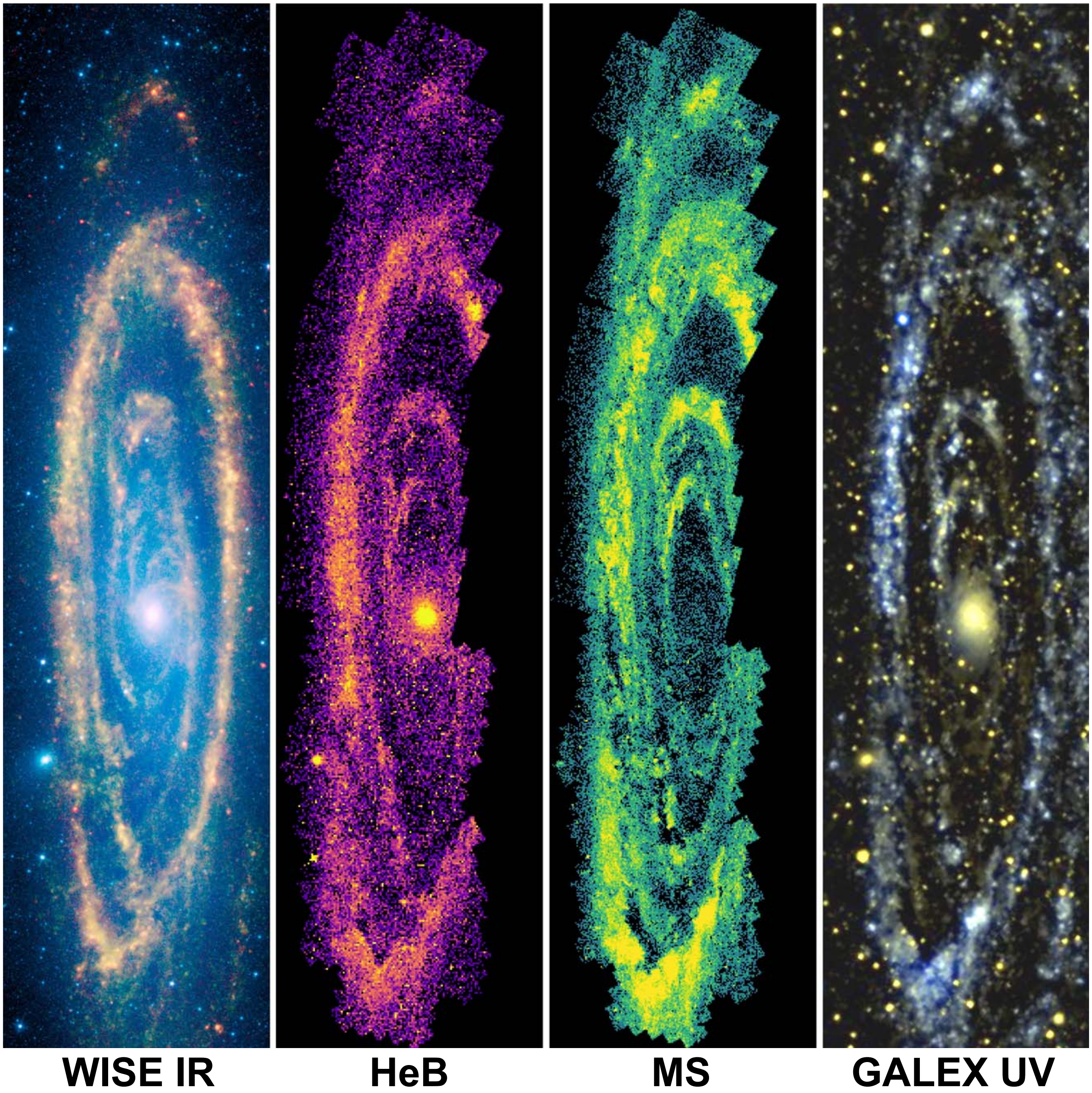

Figure 24. Stellar density maps of M31 (PHAT and PHAST) from the two younger populations of HeB and MS, compared with WISE IR and GALEX UV images. The WISE (e.g., E. L. Wright et al. 2010) IR image of M31 (Credit: NASA/JPL-Caltech/UCLA) uses all four infrared detectors (3.4 and 4.6 μm in blue; 12 μm in green; and 22 μm in red). Blue highlights relatively mature stars, while yellow and red show dust heated by newborn, massive stars. By heavily weighting the long-wavelength channels, this WISE image effectively highlights emission from PAHs, which are a significant component of the warm dust commonly found in star-forming regions. The GALEX UV image of M31 (D. A. Thilker et al. 2005) combines both the FUV (shown as blue) and NUV (shown as yellow) bands. The FUV highlights the hottest, youngest, and most massive stars and star-forming regions on the disk, along with nearby ionized gas regions traced by Hα emission. The NUV captures light from slightly older and cooler stars, including hot post-AGB stars, which trace dense older populations such as the bulge, globular clusters, and M32, as well as Milky Way foreground lower MS stars. Particularly the bulge exhibits significant brightness in the NUV due to the presence of evolved, likely metal-rich, old stars (P. Rosenfield et al. 2012), which accounts for its absence in the MS map.

satellite galaxies, which might also be responsible for the GSS seen at larger radii (R. D'Souza & E. F. Bell 2018).

Succinctly, our new ability to map different stellar populations across the disk offers new insight into the structural evolution of the M31 disk. While the detailed star formation history is currently being analyzed using the catalog (T. M. Wainer et al. 2024, in preparation; Z. Chen et al. 2024, in preparation), these maps provide a glimpse at lower time resolution, highlighting the catalog's potential for future in-depth studies of population dynamics and demographics in M31.

5. Conclusions

We have produced and published a catalog of resolved stellar photometry for over 90 million stars in the UV and optical bands of the southern half of M31's star-forming disk. This panchromatic catalog was obtained from 195 HST pointings covering approximately 0.45 deg^2 using the ACS camera for optical (F475W and F814W) and the WFC3 camera for NUV (F275W and F336W) observations. Using our newly developed CR rejection and astrometric alignment routine, the source positions in the catalog have been precisely aligned to the Gaia DR2 astrometric solution, with a 2D scatter of the matching distance distribution that peaks at 4 mas. The resulting catalog contains minimal contamination (<0.007%) from Milky Way foreground stars.

Our photometry technique was optimized for survey depth and chip gap coverage by utilizing all overlapping exposures across all bands. The photometry achieves a completeness-limited depth of F475W ∼ 27.7, F814W ∼ 26.2, F275W ∼ 24.8, and F336W ∼ 25.4 in the lowest surface density regions in the outer disk, while reaching F475W ∼ 26.0, F814W ∼ 24.0, F275W ∼ 24.6, and F336W ∼ 25.2 in the most crowded, high surface brightness regions near M31's bulge. Crowding causes the limiting magnitude to be brighter in the optical bands. We also present seamless population maps of the entire M31 disk, showing relatively well-mixed distributions for populations older than 1–2 Gyr, and highly structured distributions for younger populations.

Combined with the PHAT survey, the total catalog has nearly 0.2 billion stars, making it the largest ever produced for equidistant sources that is publicly available. This photometry catalog will enable future studies on topics such as the star formation history of M31's southern disk, the merger history and disk evolution of M31, the star cluster population, the IMF of star clusters, and many more.

We have conducted extensive quality checks on the photometry, including ensuring that the TRGB aligns with previous distance measurements of M31, and running suites of ASTs to assess precision and completeness. All of our tests, as well as our stellar density maps, suggest that the photometric quality remains homogeneous throughout the survey.

We have produced seamless stellar population maps of the entire M31 disk with the most distinct CMD features. We present both the relatively well-mixed distributions for stellar populations older than 1-2 Gyr, and highly structured distributions for younger populations. These high-quality stellar population maps serve as direct tracers, allowing us to quantify specific structures of M31's star-forming disk and map these features using individual stars for the first time. The morphology of M31's disk, as revealed by our population maps, further presents the potential for future in-depth comparisons with simulations of M31's evolution. This offers new insights into the structural evolution study of M31.

The simplified version of our photometry and AST catalogs, included with the supplemental data, will likely meet many scientific needs, but the complete photometry measurements, including all quality metrics, are available at MAST as part of a HLSP via DOI:10.17909/aa43-mt38.

Acknowledgments

Support for this work was provided by NASA through grants #GO-16778 and 16796–16801 from the Space Telescope Science Institute, which is operated by the Association of Universities for Research in Astronomy, Incorporated, under NASA contract NAS5-26555. The Flatiron Institute is funded by the Simons Foundation.

Facility: HST (ACS/WFC; WFC3/UVIS).

Software: `Astropy` (Astropy Collaboration et al. 2013, 2018), `Astroquery` (A. Ginsburg et al. 2017, 2019), `deepCR` (Z. Chen et al. 2024), `DOLPHOT` (A. E. Dolphin 2000; A. Dolphin 2016), `Drizzlepac` (STSCI Development Team 2012; W. J. Hack et al. 2013; R. J. Avila et al. 2015), `Matplotlib` (J. D. Hunter 2007), `NumPy` (S. van der Walt et al. 2011; C. R. Harris et al. 2020), `Pandas` (The pandas development Team 2022), `Seaborn` (M. Waskom et al. 2023), `SciPy` (P. Virtanen et al. 2020), and `Vaex` (M. A. Breddels & J. Veljanoski 2018).

ORCID iDs

Zhuo Chen https://orcid.org/0000-0002-3038-3896
Benjamin Williams https://orcid.org/0000-0002-7502-0597
Dustin Lang https://orcid.org/0000-0002-1172-0754
Andrew Dolphin https://orcid.org/0000-0001-8416-4093
Meredith Durbin https://orcid.org/0000-0001-7531-9815
Julianne J. Dalcanton https://orcid.org/0000-0002-1264-2006
Adam Smercina https://orcid.org/0000-0003-2599-7524
Léo Girardi https://orcid.org/0000-0002-6301-3269
Claire E. Murray https://orcid.org/0000-0002-7743-8129
Eric F. Bell https://orcid.org/0000-0002-5564-9873
Martha L. Boyer https://orcid.org/0000-0003-4850-9589
Richard D'Souza https://orcid.org/0000-0001-9269-8167
Karoline Gilbert https://orcid.org/0000-0003-0394-8377
Karl Gordon https://orcid.org/0000-0001-5340-6774
Puragra Guhathakurta https://orcid.org/0000-0001-8867-4234
Francois Hammer https://orcid.org/0000-0002-2165-5044
L. Clifton Johnson https://orcid.org/0000-0001-6421-0953
Tod R. Lauer https://orcid.org/0000-0003-3234-7247
Margaret Lazzarini https://orcid.org/0000-0003-3252-352X
Jeremiah W. Murphy https://orcid.org/0000-0003-1599-5656
Ekta Patel https://orcid.org/0000-0002-9820-1219
Amanda Quirk https://orcid.org/0000-0001-8481-2660
Mariangelly Díaz Rodríguez https://orcid.org/0000-0002-4652-5983
Julia Christine Roman-Duval https://orcid.org/0000-0001-6326-7069
Robyn E. Sanderson https://orcid.org/0000-0003-3939-3297
Anil Seth https://orcid.org/0000-0003-0248-5470
Tobin M. Wainer https://orcid.org/0000-0001-6320-2230
Daniel R. Weisz https://orcid.org/0000-0002-6442-6030

References

Akeson, R., Armus, L., Bachelet, E., et al. 2019, arXiv:1902.05569
Amendola, L., Appleby, S., Avgoustidis, A., et al. 2018, LRR, 21, 2
Anderson, J., & Bedin, L. R. 2010, PASP, 122, 1035
Anderson, J., & Ryon, J. E. 2018, Instrument Science Report ACS 2018-04, Space Telescope Science Institute
Arnaboldi, M., Bhattacharya, S., Gerhard, O., et al. 2022, A&A, 666, A109
Arp, H. 1964, ApJ, 139, 1045
Astropy Collaboration, Price-Whelan, A. M., Sipőcz, B. M., et al. 2018, AJ, 156, 123
Astropy Collaboration, Robitaille, T. P., Tollerud, E. J., et al. 2013, A&A, 558, A33
Avila, R. J., Hack, W., Cara, M., et al. 2015, in ASP Conf. Ser. 495, Astronomical Data Analysis Software an Systems XXIV (ADASS XXIV), ed. A. R. Taylor & E. Rosolowsky (San Francisco, CA: ASP), 281
Bajaj, V. 2017, Instrument Science Report WFC3 2017-19, Space Telescope Science Institute
Bajaja, E., & Shane, W. W. 1982, A&AS, 49, 745
Barker, M. K., Sarajedini, A., & Harris, J. 2004, ApJ, 606, 869
Bastian, N., Covey, K. R., & Meyer, M. R. 2010, ARA&A, 48, 339
Beaton, R. L., Bono, G., Braga, V. F., et al. 2018, SSRv, 214, 113

Bekki, K., Couch, W. J., Drinkwater, M. J., & Gregg, M. D. 2001, ApJL, 557, L39

Bernard, E. J., Ferguson, A. M. N., Richardson, J. C., et al. 2015, MNRAS, 446, 2789

Bohlin, R. C. 2016, AJ, 152, 60

Bovy, J., Rix, H.-W., & Hogg, D. W. 2012, ApJ, 751, 131

Boyer, M. L., McQuinn, K. B. W., Groenewegen, M. A. T., et al. 2017, ApJ, 851, 152

Boyer, M. L., Williams, B. F., Aringer, B., et al. 2019, ApJ, 879, 109

Breddels, M. A., & Veljanoski, J. 2018, A&A, 618, A13

Bressan, A., Marigo, P., Girardi, L., et al. 2012, MNRAS, 427, 127

Chen, Z., Zhang, K., Williams, B. F., & Durbin, M. 2024, ApJ, 962, 7

Choi, Y., Dalcanton, J. J., Williams, B. F., et al. 2020, ApJ, 902, 54

Choi, Y., Nidever, D. L., Olsen, K., et al. 2018, ApJ, 866, 90

Cignoni, M., Tosi, M., & Hopp, U. 2010, AdAst, 2010, 158568

Cioni, M. R. L., Clementini, G., Girardi, L., et al. 2011, A&A, 527, A116

Collins, M. L. M., Chapman, S. C., Ibata, R. A., et al. 2011, MNRAS, 413, 1548

Corbelli, E., Lorenzoni, S., Walterbos, R., Braun, R., & Thilker, D. 2010, A&A, 511, A89

Dalcanton, J. J., Bell, E. F., Choi, Y., et al. 2023, AJ, 166, 80

Dalcanton, J. J., Fouesneau, M., Hogg, D. W., et al. 2015, ApJ, 814, 3

Dalcanton, J. J., Williams, B. F., Lang, D., et al. 2012, ApJS, 200, 18

Deason, A. J., Belokurov, V., & Evans, N. W. 2011, MNRAS, 416, 2903

Deustua, S. E., Mack, J., Bajaj, V., & Khandrika, H. 2017, Instrument Science Report WFC3 2017-14, Space Telescope Science Institute 19

Devereux, N. A., Price, R., Wells, L. A., & Duric, N. 1994, AJ, 108, 1667

Dolphin, A. 2016, DOLPHOT: Stellar photometry, Astrophysics Source Code Library, ascl:1608.013

Dolphin, A. E. 2000, PASP, 112, 1383

Dorman, C. E., Guhathakurta, P., Seth, A. C., et al. 2015, ApJ, 803, 24

Dorman, C. E., Widrow, L. M., Guhathakurta, P., et al. 2013, ApJ, 779, 103

Drechsler, M., Strottner, X., Sainty, Y., et al. 2023, RNAAS, 7, 1

D'Souza, R., & Bell, E. F. 2018, NatAs, 2, 737

Elia, D., Molinari, S., Schisano, E., et al. 2022, ApJ, 941, 162

Escala, I., Gilbert, K. M., Kirby, E. N., et al. 2020, ApJ, 889, 177

Escala, I., Gilbert, K. M., Wojno, J., Kirby, E. N., & Guhathakurta, P. 2021, AJ, 162, 45

Escala, I., Quirk, A. C. N., Guhathakurta, P., et al. 2023, AJ, 165, 75

Fardal, M. A., Babul, A., Geehan, J. J., & Guhathakurta, P. 2006, MNRAS, 366, 1012

Fardal, M. A., Guhathakurta, P., Babul, A., & McConnachie, A. W. 2007, MNRAS, 380, 15

Fardal, M. A., Weinberg, M. D., Babul, A., et al. 2013, MNRAS, 434, 2779

Gallart, C. 1998, ApJL, 495, L43

Gallart, C., Zoccali, M., & Aparicio, A. 2005, ARA&A, 43, 387

Gibson, B. J., Zasowski, G., Seth, A., et al. 2023, ApJ, 952, 23

Ginsburg, A., Parikh, M., Woillez, J., et al. 2017, Astroquery: Access to Online Data Resources, Astrophysics Source Code Library, ascl:1708.004

Ginsburg, A., Sipőcz, B. M., Brasseur, C. E., et al. 2019, AJ, 157, 98

Girardi, L., Barbieri, M., Groenewegen, M. A. T., et al. 2012, in Red Giants as Probes of the Structure and Evolution of the Milky Way, ed. A. Miglio, J. Montalbán, & A. Noels, Vol. 26 (Berlin: Springer), 165

Girardi, L., Groenewegen, M. A. T., Hatziminaoglou, E., & da Costa, L. 2005, A&A, 436, 895

Gordon, K. D., Bailin, J., Engelbracht, C. W., et al. 2006, ApJL, 638, L87

Gordon, K. D., Fouesneau, M., Arab, H., et al. 2016, ApJ, 826, 104

Haas, M., Lemke, D., Stickel, M., et al. 1998, A&A, 338, L33

Habing, H. J., Miley, G., Young, E., et al. 1984, ApJL, 278, L59

Hack, W. J., Dencheva, N., & Fruchter, A. S. 2013, in ASP Conf. Ser. 475, Astronomical Data Analysis Software and Systems XXII, ed. D. N. Friedel (San Francisco, CA: ASP), 49

Hammer, F., Yang, Y. B., Wang, J. L., et al. 2018, MNRAS, 475, 2754

Harris, C. R., Millman, K. J., van der Walt, S. J., et al. 2020, Natur, 585, 357

Harris, J., & Zaritsky, D. 2004, AJ, 127, 1531

Harris, J., & Zaritsky, D. 2009, AJ, 138, 1243

Henze, M., Darnley, M. J., Williams, S. C., et al. 2018, ApJ, 857, 68

Howley, K. M., Guhathakurta, P., van der Marel, R., et al. 2013, ApJ, 765, 65

Hunter, J. D. 2007, CSE, 9, 90

Ibata, R., Irwin, M., Lewis, G., Ferguson, A. M. N., & Tanvir, N. 2001, Natur, 412, 49

Ibata, R., Martin, N. F., Irwin, M., et al. 2007, ApJ, 671, 1591

Ibata, R. A., Lewis, G. F., McConnachie, A. W., et al. 2014, ApJ, 780, 128

Johnson, L. C., Seth, A. C., Dalcanton, J. J., et al. 2015, ApJ, 802, 127

Johnson, L. C., Seth, A. C., Dalcanton, J. J., et al. 2017, ApJ, 839, 78

Krist, J. E., Hook, R. N., & Stoehr, F. 2011, Proc. SPIE, 8127, 81270J

Kroupa, P. 2001, MNRAS, 322, 231

Lewis, A. R., Dolphin, A. E., Dalcanton, J. J., et al. 2015, ApJ, 805, 183

Lewis, A. R., Simones, J. E., Johnson, B. D., et al. 2017, ApJ, 834, 70

Marigo, P., Girardi, L., Bressan, A., et al. 2008, A&A, 482, 883

Marigo, P., Girardi, L., Bressan, A., et al. 2017, ApJ, 835, 77

McConnachie, A. W. 2012, AJ, 144, 4

McConnachie, A. W., Irwin, M. J., Ferguson, A. M. N., et al. 2005, MNRAS, 356, 979

McQuinn, K. B. W., Skillman, E. D., Cannon, J. M., et al. 2010, ApJ, 721, 297

Monachesi, A., Trager, S. C., Lauer, T. R., et al. 2011, ApJ, 727, 55

Mutch, S. J., Croton, D. J., & Poole, G. B. 2011, ApJ, 736, 84

Nakanishi, H., & Sofue, Y. 2003, PASJ, 55, 191

Peltonen, J., Rosolowsky, E., Johnson, L. C., et al. 2023, MNRAS, 522, 6137

Perina, S., Barmby, P., Beasley, M. A., et al. 2009, A&A, 494, 933

Quirk, A., Guhathakurta, P., Chemin, L., et al. 2019, ApJ, 871, 11

Rice, W. 1993, AJ, 105, 67

Robitaille, T. P., & Whitney, B. A. 2010, ApJL, 710, L11

Rosenfield, P., Johnson, L. C., Girardi, L., et al. 2012, ApJ, 755, 131

Rosenfield, P., Marigo, P., Girardi, L., et al. 2014, ApJ, 790, 22

Sabbi, E., Sirianni, M., Nota, A., et al. 2007, AJ, 133, 44

Schlafly, E. F., & Finkbeiner, D. P. 2011, ApJ, 737, 103

Schneider, R., Valiante, R., Ventura, P., et al. 2014, MNRAS, 442, 1440

Skillman, E. D., Tolstoy, E., Cole, A. A., et al. 2003, ApJ, 596, 253

Smercina, A., Dalcanton, J. J., Williams, B. F., et al. 2023, ApJ, 957, 3

Stilp, A. M., Dalcanton, J. J., Skillman, E., et al. 2013, ApJ, 773, 88

STSCI Development Team 2012, DrizzlePac: HST Image Software, Astrophysics Source Code Library, ascl:1212.011

Telford, O. G., Dalcanton, J. J., Williams, B. F., et al. 2020, ApJ, 891, 32

Telford, O. G., Werk, J. K., Dalcanton, J. J., & Williams, B. F. 2019, ApJ, 877, 120

The pandas development Team 2022, pandas-dev/pandas: Pandas, v2.2.2, Zenodo, doi:10.5281/zenodo.3509134

Thilker, D. A., Hoopes, C. G., Bianchi, L., et al. 2005, ApJL, 619, L67

Tolstoy, E., Hill, V., & Tosi, M. 2009, ARA&A, 47, 371

van der Walt, S., Colbert, S. C., & Varoquaux, G. 2011, CSE, 13, 22

Virtanen, P., Gommers, R., Oliphant, T. E., et al. 2020, NatMe, 17, 261

Waskom, M., Gelbart, M., Botvinnik, O., et al. 2023, mwaskom/seaborn: v0.13.0 (September 2023), Zenodo, doi:10.5281/zenodo.592845

Weisz, D. R., Dalcanton, J. J., Williams, B. F., et al. 2011, ApJ, 739, 5

Weisz, D. R., Johnson, L. C., Foreman-Mackey, D., et al. 2015, ApJ, 806, 198

Williams, B. F. 2003, AJ, 126, 1312

Williams, B. F., Dalcanton, J. J., Bell, E. F., et al. 2015, ApJ, 802, 49

Williams, B. F., Dalcanton, J. J., Dolphin, A. E., Holtzman, J., & Sarajedini, A. 2009a, ApJL, 695, L15

Williams, B. F., Dalcanton, J. J., Seth, A. C., et al. 2009b, AJ, 137, 419

Williams, B. F., Dolphin, A. E., Dalcanton, J. J., et al. 2017, ApJ, 846, 145

Williams, B. F., Durbin, M., Lang, D., et al. 2023, ApJS, 268, 48

Williams, B. F., Durbin, M. J., Dalcanton, J. J., et al. 2021, ApJS, 253, 53

Williams, B. F., Lang, D., Dalcanton, J. J., et al. 2014, ApJS, 215, 9

Wright, E. L., Eisenhardt, P. R. M., Mainzer, A. K., et al. 2010, AJ, 140, 1868

Zhang, K., & Bloom, J. S. 2020, ApJ, 889, 24